SUPERHYDROPHOBIC SURFACE:

DESIGN, FABRICATION, AND APPLICATIONS

by

Liangliang Cao

B.S., Zhengzhou University, China, 2002

M.S., Zhejiang University, China, 2005

Submitted to the Graduate Faculty of

Swanson School of Engineering in partial fulfillment

of the requirements for the degree of

Doctor of Philosophy

University of Pittsburgh

2010

UNIVERSITY OF PITTSBURGH

SWANSON SCHOOL OF ENGINEERING

This dissertation was presented

by

Liangliang Cao

It was defended on

September 16, 2010

and approved by

William J. Federspiel, Professor, Departments of Chemical and Petroleum Engineering, Surgery, Bioengineering, Swanson School of Engineering

Sachin S. Velankar, Associate Professor, Department of Chemical and Petroleum Engineering, Swanson School of Engineering

Sung Kwon Cho, Associate Professor, Department of Mechanical Engineering and Materials Science, Swanson School of Engineering

Dissertation Director: Di Gao, Assistant Professor, Department of Chemical and Petroleum Engineering, Swanson School of Engineering

SUPERHYDROPHOBIC SURFACE:

DESIGN, FABRICATION, AND APPLICATIONS

Liangliang Cao, Ph.D.

University of Pittsburgh, 2010

Superhydrophobic surfaces are often found on plant leaves and insect wings in nature. Water on these surfaces forms small beads with a high contact angle of greater than 150° and drips off rapidly when the surfaces are slightly inclined. This interesting phenomenon has stimulated extensive research to make artificial superhydrophobic surfaces and to employ them for a variety of applications. A key challenge in making superhydrophobic surfaces is to tailor the morphology of the surfaces in nanometer scales, which typically involves synthesis and fabrication of materials at nanometer dimensions.

In this dissertation, I will first explain general design principles for fabricating superhydrophobic surfaces, with a specific focus on how to fabricate superhydrophobic surfaces on intrinsically hydrophilic materials. I will then present several fabrication methods developed during my Ph.D. program for making artificial superhydrophobic surfaces following such design principles. Finally, I will discuss initial results of our investigation on two promising applications of superhydrophobic surfaces, namely, for anti-icing and hydrodynamic drag reduction purposes, respectively.

TABLE OF CONTENTS

LIST OF TABLES

LIST OF FIGURES

ACKNOWLEDGEMENTS

First I would like to express my sincere appreciation to my advisor, Prof. Di Gao, for his constant guidance, support, and discussion throughout my PhD research work. He is a wonderful person and a great mentor. It has been my great pleasure working in his group.

I would also like to thank my committee members, Prof. William J. Federspiel, Prof. Sachin S. Velankar, and Prof. Sung Kwon Cho, for your time and constructive suggestion for this thesis.

Furthermore, I would like to thank all my group members, Jiamin Wu, Ashish Yeri, Umang Desai, Dr. Lizeng Gao, Dr. Chengkun Xu, and Dr. Anmin Cao, for your great help in my research. Also，we had lots of fun in the lab, which made the research work more productive and enjoyable.

Finally, I would like to dedicate my thesis to my parents, my lovely daughter Iris, and my wife Jianxia Liu. Without her support, encouragement, and care, I really cannot imagine what I could be right now. She has turned my life into a totally different and positive way, and let me have a great journey during my PhD process or even all my life.

1.0 INTRODUCTION

1.1 SUPERHYDROPHOBIC SURFACES IN NATURE

Superhydrophobic surfaces are often found in nature, such as on plant leaves [1-3], insect legs [4] and wings [5]. Water on these surfaces forms small beads with a high contact angle in excess of 150 °and drips off rapidly when the surfaces are slightly inclined, while taking away powder-like contaminant. This interesting phenomenon has stimulated extensive research to make artificial superhydrophobic surfaces and to use them for a variety of applications.

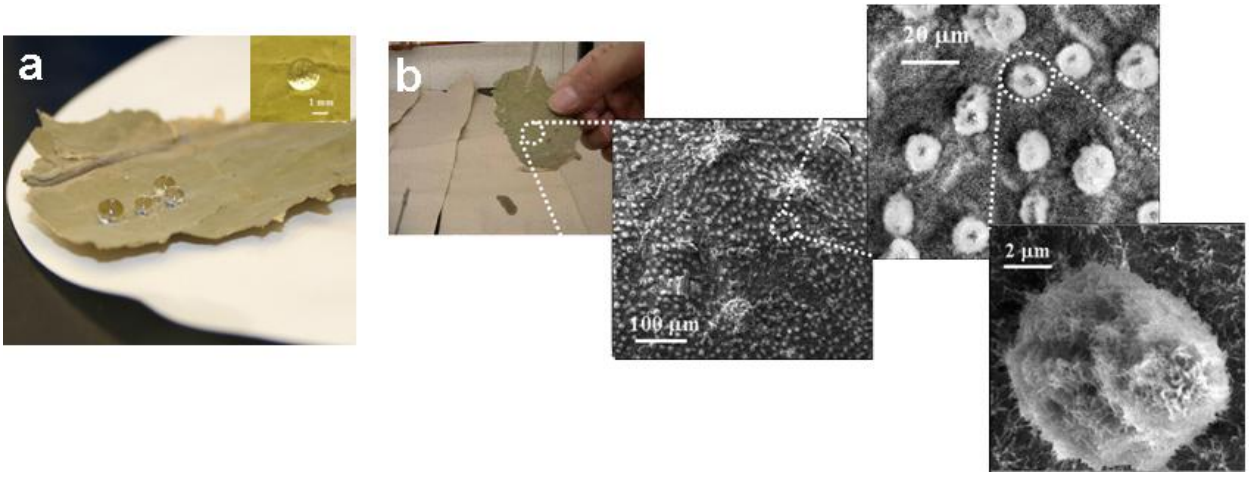

Figure 1. Superhydrophobic surfaces on lotus leaves. (a) Water droplets on the lotus leaf. (b) Typical SEM images of the surface structures on the lotus leaf.

The concept of superhydrophobic surfaces is originally drawn from the inspiration of lotus leaves in nature. Therefore, the very high water repellency (superhydrophobicity) and the self-cleaning properties exhibited by the lotus leaf have been referred to as "lotus effect", which has been attributed to a combined effect of the hydrophobicity induced by the epicuticular wax and the surface roughness resulted from the hierarchical structures on the leaf (Fig. 1).

1.2 WETTING ON SURFACES

1.2.1 Wetting on flat surfaces

When a liquid droplet is deposited on a chemically homogenous and physically flat (or smooth) solid surface (Fig. 2), the surface wettability is mainly determined by the surface chemical composition. The liquid contact angle on the flat surface (or the intrinsic water contact angle, θ_{flat}) can be correlated to three interfacial free energies, *i.e.*, free energies at the solid-air (γ_{SV}), solid-liquid (γ_{SL}) and liquid-air (γ_{LV}) interfaces, by the Young's equation:

$$\cos\theta_{flat} = \frac{\gamma_{SV} - \gamma_{SL}}{\gamma_{LV}}, \qquad (1)$$

where γ_{SL} can be estimated by [6]

$$\gamma_{SL} = \gamma_{SV} + \gamma_{LV} - 2\sqrt{\gamma_{SV} \cdot \gamma_{LV}} \ . \qquad (2)$$

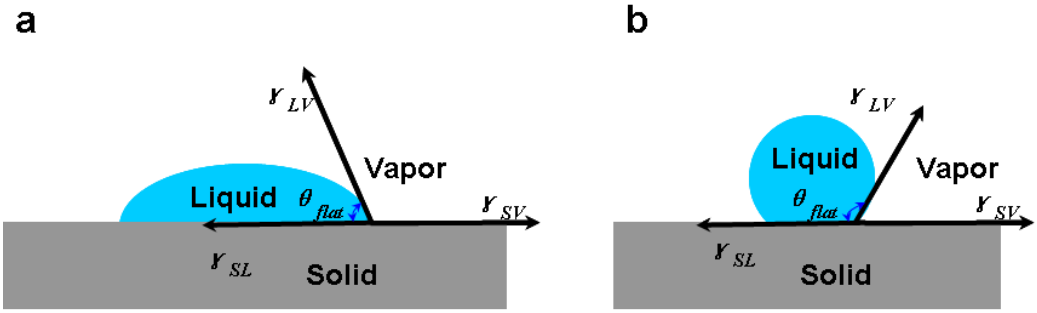

Figure 2. Contact angle of a liquid on an ideally flat surface (Young's model). For water, if $\theta_{flat} < 90°$, it is an intrinsically hydrophilic surface (a); if $\theta_{flat} > 90°$, it is an intrinsically hydrophobic surface (b).

According to Eqns. (1) and (2), the surface hydrophobicity increases with decreasing the surface free energy of the solid-air interface (γ_{SV}). When θ_{flat} is smaller than 90°, the solid surface is considered intrinsically hydrophilic; when θ_{flat} is greater than 90°, the solid surface is considered intrinsically hydrophobic. The reported lowest surface free energy of the solid-air interface is possessed by the trifluoromethyl group (CF_3)-terminated surface (~ 6 mN/m) [7], with a θ_{flat} of ~ 120°, which is almost the highest water contact angle that can be obtained on a flat surface. Further increase of the hydrophobicity requires manipulation of the surface topography.

1.2.2 Wetting on rough surfaces

The effect of surface roughness on wettability was first discussed by Wenzel in 1936 [8] and then by Cassie and Baxter in 1944 [9]. Wenzel suggested that the effective surface area increases as the surface becomes rough, and hence water will tend to spread more on a rough

hydrophilic substrate to develop more solid-liquid contact, while spread less on a rough hydrophobic substrate to decrease the contact area to solid, both of which are thermodynamically more favorable. A key assumption of this conclusion is that water is in complete contact with the solid surface, which is called Wenzel state (Fig. 3a). The relationship between the apparent contact angle on a rough surface (θ_{rough}) and its intrinsic contact angle (θ_{flat}) has been described by the Wenzel equation:

$$\cos\theta_{rough} = r\cos\theta_{flat}, \qquad (3)$$

where *r* is the roughness factor, defined as the ratio of the actual surface area to its horizontal projection. Since *r* is always greater than 1 for a rough surface, this equation predicts that if $\theta_{flat} > 90°$, $\theta_{rough} > \theta_{flat}$, and if $\theta_{flat} < 90°$, $\theta_{rough} < \theta_{flat}$. Therefore, in the Wenzel state, surface roughness will make intrinsically hydrophobic surfaces more hydrophobic and intrinsically hydrophilic surfaces more hydrophilic.

However, as the surface roughness or the surface hydrophobicity increases, it becomes unlikely for water to completely follow the surface topography of a hydrophobic substrate so as to have a complete contact with the solid surface, since the system is in a higher energy state when the hydrophobic substrate is in complete contact with water than when it is only in partial contact with water. Instead, air may be trapped between water and the surface texture. As a result, water is in contact with a composite surface of solid and air, and forms droplets (known as fakir droplets). Such state is called Cassie State (Fig. 3b). The apparent contact angle in this case has been described by the Cassie-Baxter equation

$$\cos\theta_{rough} = \phi_S \cos\theta_{flat} + \phi_V \cos\theta_{LV} = \phi_S \cos\theta_{flat} - (1 - \phi_S), \qquad (4)$$

where ϕ_S and ϕ_V are the fractions of solid and air contacting the water ($\phi_S + \phi_V = 1$). Since the contact angle of water on air (θ_{LV}) is 180 °($\cos\theta_{LV} = -1$), air entrapment will remarkably increase the apparent surface hydrophobicity. Based on Eqn. 4, monotonic decrease of ϕ_S results in an increase of θ_{rough}, and eventually leads to a superhydrophobic state.

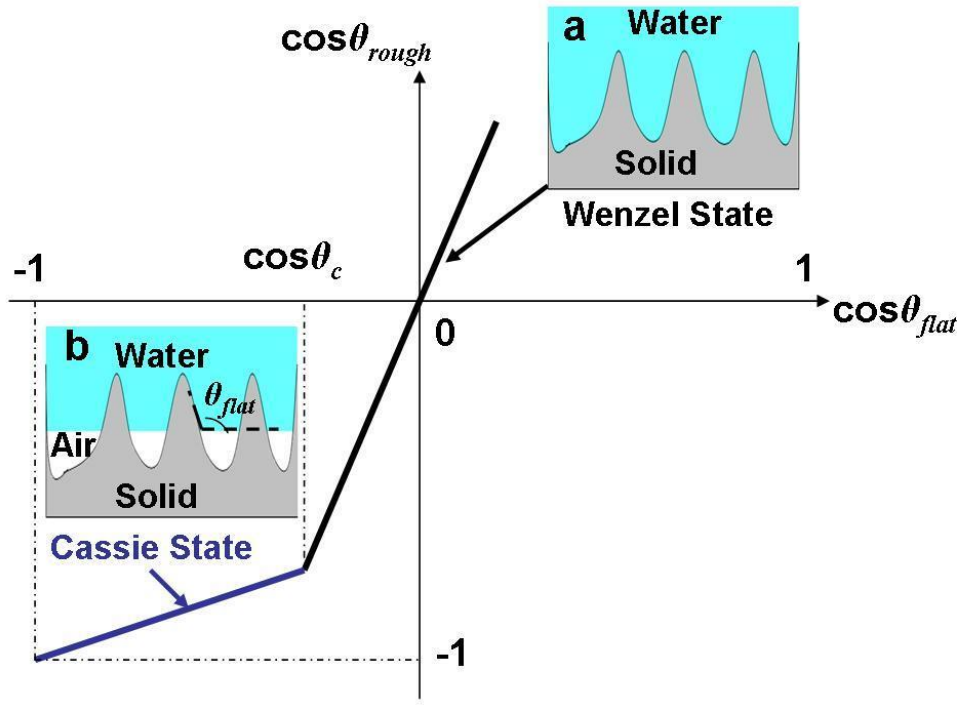

Figure 3. Relationship of $\cos\theta_{rough}$ with $\cos\theta_{flat}$. The black solid and blue solid lines correspond to the Wenzel state and the Cassie state, respectively.

For a system where water is in contact with a rough solid surface, one of the two states (Wenzel state or Cassie state) may exist. The relationship between $\cos\theta_{rough}$ and $\cos\theta_{flat}$ for these two states is plotted in Figure 3, according to Eqns. (3) and (4), as previously demonstrated [10]. The two lines corresponding to the two states intersect at one critical angle θ_c

$$\cos\theta_c = -\frac{1-\phi_S}{r-\phi_S}. \qquad (5)$$

It has been proved that the energy of the system decreases monotonically when $\cos\theta_{rough}$ increases [11]. Therefore, when water contacts a solid surface with $\theta_{flat} < \theta_c$, the Wenzel state is thermodynamically more favorable (with smaller θ_{rough} and greater $\cos\theta_{rough}$ than those in the Cassie state) and hence should be preferred by the system from a thermodynamic point of view; when water contacts a solid surface with $\theta_{flat} > \theta_c$, the Cassie state is thermodynamically more favorable. It should be noted that, according to Eqn. (5), θ_c is always greater than 90 °, since $\phi_S < 1 \text{ and } r > 1$.

1.2.3 Contact angle hysteresis

In addition to the contact angle measured in a static manner, another parameter, contact angle hysteresis, is also important for characterizing the surface wettability. The contact angle hysteresis is the difference between the advancing and receding contact angles typically measured during expansion and contraction of the droplets induced by placing a needle in the water droplets and continuously supplying and withdrawing water through the needle. The advancing contact angle θ_A is recorded when the liquid volume reaches maximum before the

liquid-solid interfacial area starts to increase; the receding contact angle θ_R is recorded when the liquid volume reaches minimum before the interfacial area starts to decrease. Sometimes, sliding angle, which is defined as the minimum angle that the substrate needs to be tilted before a droplet starts to roll off, is also used to characterize the wettability of a surface. The relationship between the contact angle hysteresis and the sliding angle can be described by the following equation [12]:

$$mg(\sin\alpha)/w = \gamma_{lv}(\cos\theta_R - \cos\theta_A), \qquad (6)$$

where α is the sliding angle, *g* is the acceleration due to gravity, *m* is the mass of the droplet, and *w* is the diameter of the wetting area. From Eqn. 6, it can be seen that the sliding angle depends on the mass or the size of the droplet and for the same sized droplet, small contact angle hysteresis will lead to a small sliding angle. Therefore, sliding angle can be used to compare the wettability of two surfaces only when the same sized droplet is used, and the contact angle hysteresis is a better parameter for the purpose of characterizing the surface wettability. Typical superhydrophobic surfaces should have a static water contact angle of greater than 150 º and contact angle hysteresis of smaller than 10 º.

1.3 CONVENTIONAL FABRICATION OF SUPERHYDROPHOBIC SURFACES

To date, a wide variety of physical and chemical methods have been explored to fabricate superhydrophobic surfaces through one of the following two approaches: (i) creating a rough surface on a hydrophobic material or (ii) modifying a rough surface with a hydrophobic coating.

1.3.1 Creating a rough surface on a hydrophobic material

In this approach, hydrophobic polymers are typically used as the substrate to obtain superhydrophobicity. By making the surfaces of the polymer materials rough, the superhydrophobic behavior can be readily observed. Onda *et al.* prepared a super-water-repellent fractal surface by solidifying the melted alkylketene dimmer (AKD, a kind of wax) (Fig. 4a) [13]. It has been demonstrated that the contact angle of a liquid droplet placed on a fractal surface can be expressed as a function of the fractal dimension, the range of fractal behavior, and the contacting ratio of the surface. Jin *et al.* reported a laser etching method to make superhydrophobic polydimethylsiloxane (PDMS) surface, which contains micro-, submicro- and nano-composite structures (Fig. 4b) [14]. The water contact angle for the etched PDMS surface is higher than 160 ° and sliding angle is lower than 5 °. Ma *et al.* made a superhydrophobic membrane in the form of a nonwoven fiber mat by electrospinning a PS-PDMS block polymer blended with PS homopolymer (Fig. 4c) [15]. The superhydrophobicity is attributed to the combined effect of surface enrichment in siloxane and surface roughness of the electrospun mat itself. Phase separation has also been utilized to make superhydrophobic surfaces. Erbil *et al.* prepared a superhydrophobic gel-like porous popypropylene coating by casting the polymer solution, where nonsolvents were used in conjunction with p-xylene solvent as a polymer precipitator to increase the extent of polymer phase separation (Fig. 4d) [16]. Zhang *et al.* demonstrated the fabrication of 2-D arrays of nanopillars made from perfluoropolyether derivatives using a porous anodic aluminum oxide membrane as a template (Fig. 4e). Both nanopillars on a flat surface and on a lotus-leaf-like topology exhibit superhydrophobcity, low contact angle hysteresis, and self-cleaning properties [17]. Yan *et al.* fabricated superhydrophobic poly(alkylpyrrole) films by a electrochemical synthesis method (Fig. 4f). The

film surface consists of thousands of "needle"-like microstructures in a perpendicular alignment [18].

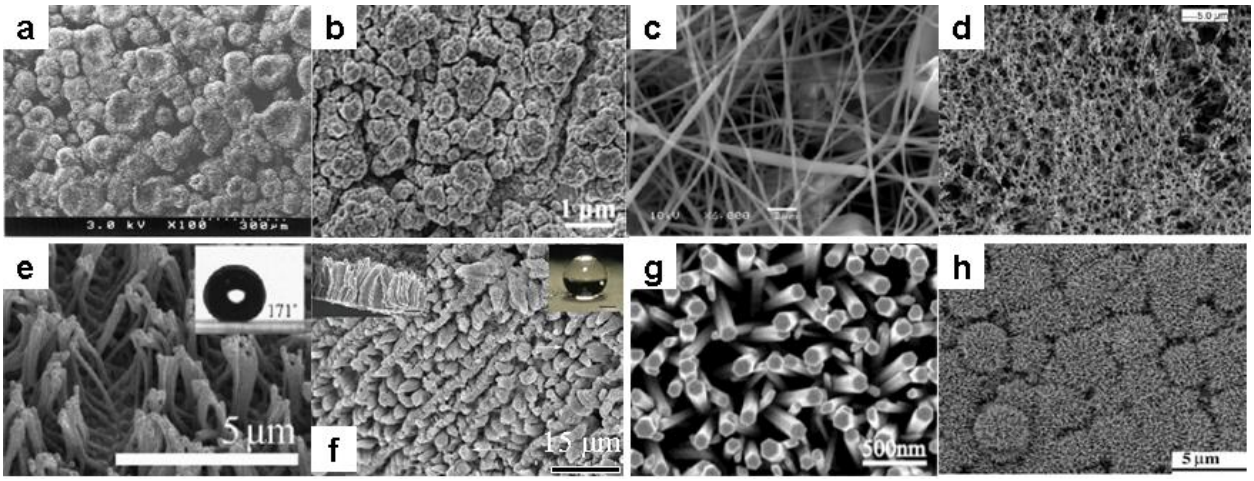

Figure 4. Representative SEM images of superhydrophobic surfaces on rough hydrophobic materials. (a) fractal AKD surface [13]; (b) laser-etched PDMS surface [14]; (c) PS-PDMS/PS electrospun fiber mat [15]; (d) i-PP coatings obtained by phase separation [16]; (e) PFPE-SS nanopillar film peeled from the p-AAO membrane [17]; (f) rough poly(alkylpyrrole) film made by electrochemical synthesis [18]; (g) aligned ZnO nanorods prepared by a two-step solution approach [19]; (h) TiO_2 nanorod films [20].

Furthermore, certain inorganic materials have also been employed in the fabrication of superhydrophobic surfaces. Feng *et al.* synthesized aligned ZnO nanorods via a two-step solution approach (Fig. 4g). The ZnO nanorods films exhibit superhydrophobicity which is due to the surface roughness and the low surface energy of the (001) plane of the nanorods exposed on the film surface. More interestingly, reversible superhydrophobicity to superhydrophilicity transition was observed and well controlled on the ZnO nanorod films by alternation of UV illumination and dark storage [19]. A similar result was also obtained on the TiO_2 nanorod films from their following work (Fig. 4h) [20].

1.3.2 Modifying a rough surface with hydrophobic coatings

Although it is a relatively simple and one-step process to make superhydrophobic surfaces by using intrinsically hydrophobic materials, unfortunately, many materials do not possess a low enough surface free energy to be intrinsically hydrophobic. In order to make superhydrophobic surfaces on these intrinsically hydrophilic materials, a two-step process is usually required, *i.e.*, making a rough surface first and then modifying it with chemicals, such as alkanethiols, organic silanes, and fatty acids, which can offer a low surface free energy after linked to the surface.

Because of the well established micro- and nano-fabrication technologies on silicon substrate, silicon has been widely used for making superhydrophobic surfaces through fabrication of a variety of surface structures. Oner and McCarthy investigated the wettability of patterned silicon surfaces (Fig. 5a), which were prepared by photolithography, followed by surface modification using silanization chemistry [21]. Water droplets moved very rapidly on these surfaces and rolled off when the substrate is slightly tilted. Baldacchini *et al* reported a way to create micro/nanoscale roughness on silicon wafers by using a femtosecond laser to etch the silicon wafers (Fig. 5b) [22]. The resultant surfaces were coated with a layer of fluoroalkylsilane molecules to yield contact angles of higher than 160 °and negligible hysteresis. Verplanck *et al.* made silicon nanowires on Si/SiO_2 substrates through a vapor-liquid-solid (VLS) mechanism (Fig. 5c) [23]. The resulting rough surfaces were modified with a fluoropolymer C_4F_8, and exhibited superhydrophobicity.

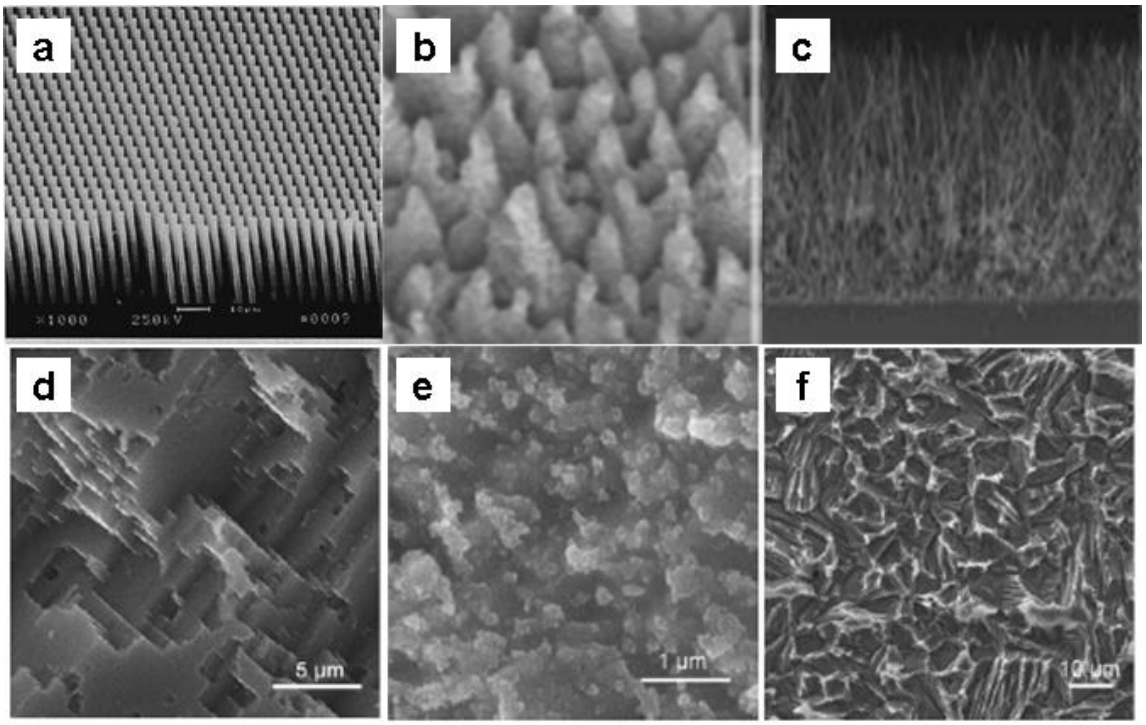

Figure 5. SEM images of superhydrophobic surfaces fabricated by coating hydrophilic micro- and nano-structures with a hydrophobic coating. (a) silicon pillar arrays fabricated by photolithography [21]; (b) silicon surfaces etched by a femtosecond laser [22]; (c) silicon nanowires grown on Si/SiO_2 substrate [23]; (d) etched aluminum surface [24]; (e) etched copper surface [24]; (f) etched zinc surface [24].

Metal surfaces can be made superhydrophobic by first etching the surfaces to obtain roughness in both micrometer and nanometer scales and then modifying the roughened surfaces with a hydrophobic coating. Qian *et al.* have made superhydrophobic surfaces on aluminum, copper, and zinc polycrystalline substrates by first using chemical etching methods and then coating the substrates with a fluoroalkysilane [24]. The key to the etching technique is the use of a dislocation etchant that preferentially dissolves the dislocation sites in the grains. The etched metallic surfaces, after modified with the fluoroalkylsilane, exhibited superhydrophobic properties with water contact angles of larger than 150 °, as well as sliding angles of less than 10 °.

Electrochemical methods have also been employed to make superhydrophobic surfaces on metal substrates. Zhang et al. described the use of polyelectrolyte multilayers in electrochemical deposition to adjust the morphology of gold clusters for fabrication of superhydrophobic surfaces [25]. They also fabricated a branchlike structure of silver aggregates by electrodeposition techniques. After modification with a self-assembled monolayer of *n*-dodecanethiol, the surface became superhydrophobic [26].

1.4 CHALLENGES

As discussed above, both of the current approaches for fabrication of superhydrophobic surfaces require a solid surface with a low enough free energy and hence an intrinsic water contact angle (θ_{flat}) of greater than 90° to further enhance the hydrophobicity by tailoring the surface roughness. Processes for obtaining a low surface free energy typically involve modifying the surfaces with organic chemical coatings. However, the hydrophobicity of chemically treated surfaces deteriorates over time, which brings major problems to the artificial superhydrophobic surfaces—aging and decay.

Another challenge to the self-cleaning property of superhydrophobic surfaces is oil contamination—these surfaces repel water but not oil. Following Eqns. (1) and (2), to achieve a θ_{flat} of greater than 90°, a γ_{SV} of less than ~ 20 mN/m is needed for water (with a γ_{LV} of ~72 mN/m), and a γ_{SV} of less than ~ 6 mN/m is needed for most alkanes with a γ_{LV} of 20-30 mN/m. If a θ_{flat} of greater than 90° is indeed needed to increase the contact angle by roughening the surface, then very few materials can be used to make super oil-repellent surfaces. For example,

Teflon is known to possess a low γ_{SV} (~ 18.5 mN/m) among most commonly used materials, but it still does not satisfy the requirement (γ_{SV} needs to be less than ~ 6 mN/m) to make it super oil-repellent (or superoleophobic). (CF_3)-terminated surfaces (with a γ_{SV} of ~ 6 mN/m), in principle, can barely satisfy this requirement. However, to experimentally obtain (CF_3)-terminated surfaces with such low γ_s has been proven challenging. Therefore, although super oil-repellent surfaces have been reported, the oil contact angles in the literature are often reported using oils with a relatively high γ_{LV} (> 30 mN/m) such as polyols, esters, arenes, and/or their mixtures [27, 28]. As a matter of fact, surfaces that possess a contact angle of greater than 150 ° for alkanes (such as hexadecane) with γ_{LV} between 20 and 30 mN/m have rarely been reported before our work. The surface tension values for some common test liquids are listed in Table 1.

A question of significant interest is whether one is able to produce a superhydrophobic surface using materials with a θ_{flat} of less than 90 °because this implies the possibility of making intrinsically hydrophilic materials superhydrophobic or even making intrinsically oleophilic materials superoleophobic. As a matter of fact, nature has provided a positive answer to this question by the fact that some leaves with an absence of hydrophobic waxes are also superhydrophobic [29]. Recent research has also found that the wax on lotus leaves has a θ_{flat} of ~74 °, in contrast to the expected value of greater than 90 °[30]. One focus of this dissertation is to elucidate the fundamental mechanisms underlying this interesting surface phenomenon, and to develop design principles and fabrication methods for making superhydrophobic surfaces on intrinsically hydrophilic materials as well as for making superoleophobic surfaces on intrinsically oleophilic materials.

Table 1. Surface tension values for some common test liquids [31].

Liquid	**Surface tension @ 20 ℃ in mN/m**	**Liquid**	**Surface tension @ 20 ℃ in mN/m**
Mercury	425.41	Cyclopentanol	32.7
Water (WA)	72.8	n-Propylbenzene	28.99
Glycerol (GLY)	64	m-Xylene	28.9
Formamide (FA)	58.2	Benzene	28.88
Diiodomethane (DI)	50.8	1-Decanol	28.5
Ethylene glycol (EG)	47.7	Toluene	28.4
Polyethylen glycol 200 (PEG)	43.5	1-Octanol	27.6
N,N-dimethyl acetamide (DMA)	36.7	Chloroform	27.5
Pyrrol (PY)	36.6	n-Hexadecane	27.47
Chloro benzene	33.6	Acetone	25.2

2.0 METASTBALE CASSIE STATE

The presence and potential importance of the metastable Cassie state have been discussed previously [32-35], where Fakir droplets in the Cassie state were observed on the surfaces consisting of high density textures when $90^o < \theta_{flat} < \theta_c$. Such a metastable Cassie state is represented by the dotted line as an extension of the solid line representing the Cassie state in Figure 6 [10]. A question that remains is if the metastable Cassie state may also exist when $\theta_{flat} < 90^o$ ($i.e., \cos\theta_{flat} > 0$), as represented by the dashed lines in the fourth quadrant of Figure 6. If possible, this suggests that one can take advantage of the metastable Cassie state to make superhydrophobic surfaces on intrinsically hydrophilic materials or even superoleophobic surfaces on intrinsically oleophilic materials. Although, as early as 2000, Herminghaus has already conceptually predicated the possibility of the existence of metastable Cassie state when $\theta_{flat} < 90^o$ which may arise from certain special surface topography such as overhang structures [36], it has not been experimentally demonstrated prior to our work.

A necessary condition for observing the metastable Cassie state is the existence of an energy barrier that separates the Wenzel state and the Cassie state. In our design principle, this energy barrier may be provided by a capillary force that prevents liquids from entering the indents present on the surface. In the case of $\theta_{flat} < 90^o$, overhang structures are needed to provide positions for the liquid-solid contact line to suspend liquids above the bottom surface.

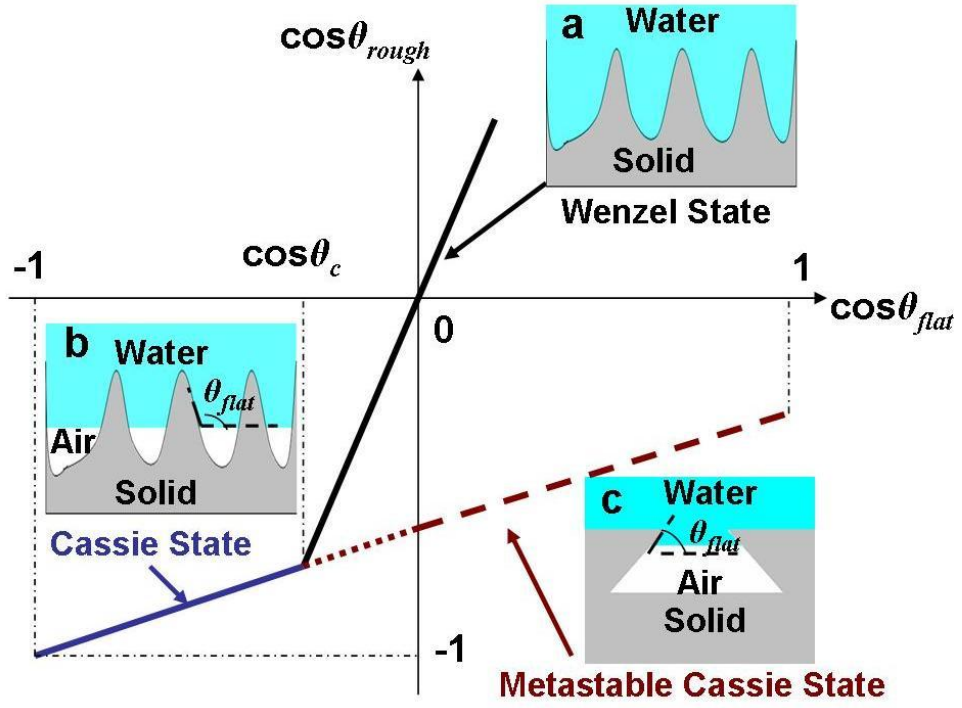

Figure 6. Relationship of $\cos\theta_{rough}$ with $\cos\theta_{flat}$. The dotted and dashed lines correspond to the metastable Cassie state when $\cos\theta_{flat} > 90°$ and the metastable Cassie state when $\cos\theta_{flat} < 90°$, respectively.

Figure 7 shows three possible cross-sectional profiles for water in contact with a solid indent consisting of overhangs. A critical parameter for these different profiles is the angle ($\theta_{overhang}$) formed between the sidewalls of the indent and the horizontal line. When $\theta_{overhang}$ is greater than θ_{flat} of the sidewall surface (Fig. 7a), the water-air interface (meniscus) inside the indent is concave when viewed from the water side. The net force generated by the meniscus (F_s) is toward the inside of the indent, causing water to enter the indent and have complete contact with

the solid (Wenzel state). When $\theta_{overhang} = \theta_{flat}$ (Fig. 7b), the water-air interface is flat and stays at a circular intersection of the indent assuming the gravity is ignored. When $\theta_{overhang} < \theta_{flat}$ (Fig. 7c), the water-air interface inside the indent is convex, and F_s is toward the outside of the indent, which prevents water from entering into the indent (Cassie state). Therefore, when $\theta_{flat} < 90^{o}$, the metastable Cassie state is only possible, if $\theta_{overhang}$ is smaller than θ_{flat}.

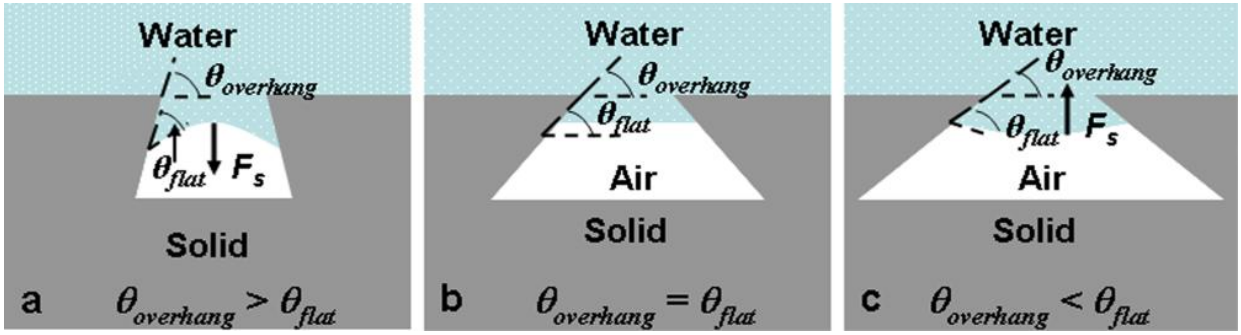

Figure 7. Three cross-sectional profiles of water in contact with a solid indent consisting of overhang structures.

3.0 FABRICATION OF SUPERHYDROPHOBIC AND SUPEROLEOPHOBIC SURFACES ON INTRINSICALLY HYDROPHILIC AND OLEOPHILIC MATERIALS

3.1 SUPERHYDROPHOBIC SURFACES ON INTRINSICALLY HYDROPHILIC SILICON PILLARS

In this section, we report the design and fabrication of micro-textures for inducing a superhydrophobic behavior on hydrogen (H)-terminated silicon surfaces with a θ_{flat} of ~74°. The micro-textures consist of overhangs with well-defined geometries fabricated by micro- and nano-fabrication technologies, which provide positions to support water and prevent water from entering the indents between the textures. As a result, water is in contact with a composite surface of solid and air, which induces the observed macroscopic superhydrophobic behavior.

3.1.1 Experimental design and methodology

We fabricate micro-textures consisting of overhang structures with well-defined geometries in both micrometer and nanometer scales. Figure 8 schematically shows the process flow to fabricate the micrometer-sized Si pillars with overhangs at the top edges. We started with Si (100) wafer coated with a 0.5 μm thermally-grown silicon dioxide (SiO_2) thin film. The SiO_2 film was patterned by photolithography, followed by wet etching in HF aqueous solution. A

Bosch deep reactive ion etching (DRIE) process using inductively coupled plasma was employed to etch the SiO_2-masked Si substrate, which formed arrays of Si pillars with vertical sidewalls. By aligning the square patterns of the Si pillars with the Si (100) wafer flat, the Si (110) surfaces were exposed on the four sidewalls of each pillar after this process. The exposed Si (110) sidewalls were then etched in a potassium hydroxide (KOH) aqueous solution (30% by weight) at 75 ℃ for 3 minutes. Etching of Si by KOH was anisotropic, which exposed (111) surfaces on the sidewalls of the Si pillars. The exposed Si (111) surface underneath the top SiO_2 mask formed overhanging sidewalls at an angle ($\theta_{overhang}$) of 54.7 ° to the top Si (100) surfaces. The SiO_2 mask was removed by HF afterwards, leaving a H-terminated Si surface.

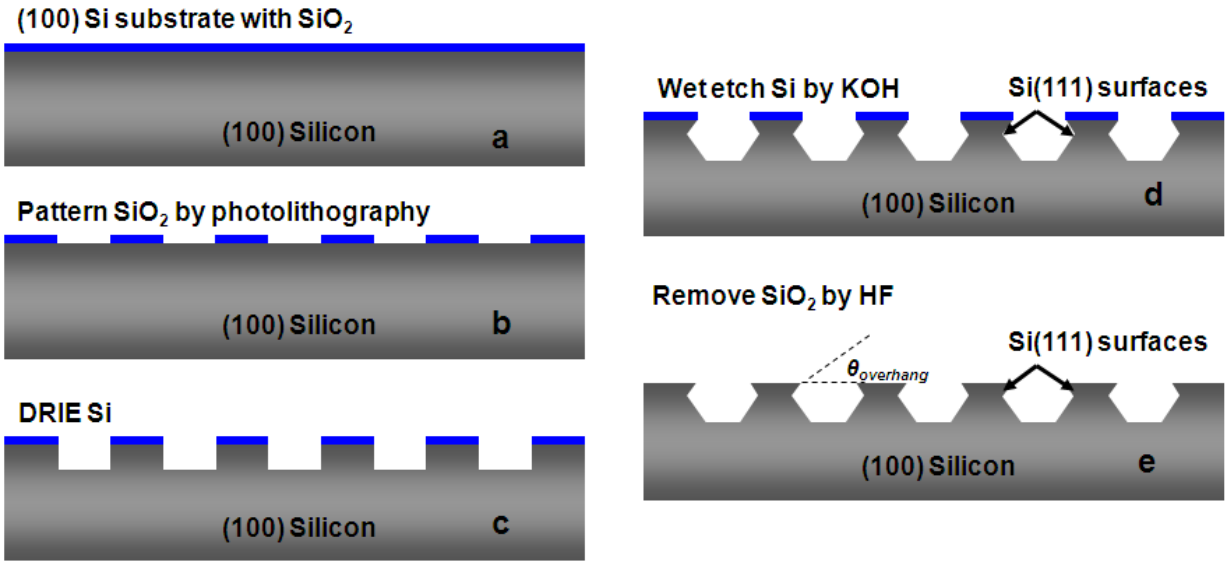

Figure 8. Schematic process flow to fabricate the micrometer-sized Si pillars with overhangs at the top edges.

Figure 9 schematically shows the top view of the design for the Si pillars. The pattern is a two-dimensional array of squares, which is 1 cm wide and 1 cm long. The critical parameters

are the width of each square (a) and the center-to-center distance between adjacent squares (x). In the mask design for photolithography, a is fixed at 10 μm, and x is varied from 13 to 30 μm. When the pattern of the photoresist was transferred to the underneath SiO_2 layer, the size of the squares decreased due to the isotropic etching of the SiO_2 by HF aqueous solution. The actual size of the squares was determined from the scanning electron microscopy (SEM) images taken afterwards. The center-to-center distance of the squares remained unchanged during the pattern transfer. These parameters and the corresponding ϕ_s (the area fraction of the solid surface in contact with water) are listed in Table 2.

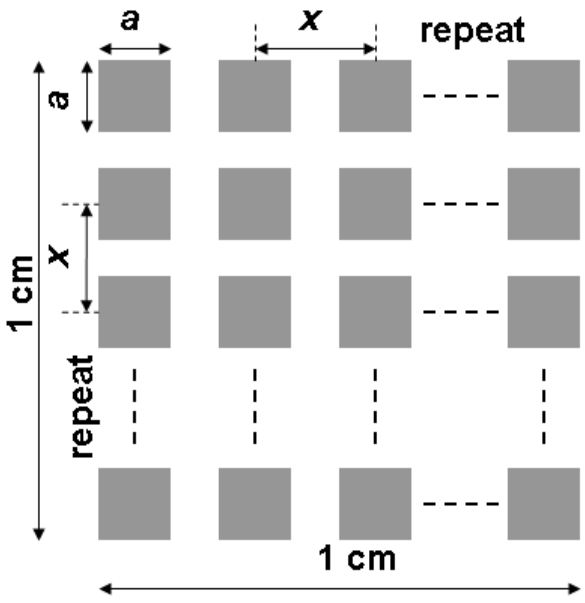

Figure 9. Design schematics for the Si pillar pattern.

Table 2. Design parameters for the Si pillar arrays.

width of each square: *a* (μm)		**center-to-center distance between adjacent squares: *x* (μm)**		$\phi_s \approx \left(\frac{a}{x}\right)^2_{actual}$
on mask	**actual**	**on mask**	**actual**	
10	**5**	**13**	**13**	**0.148**
10	**5**	**15**	**15**	**0.111**
10	**5**	**18**	**18**	**0.077**
10	**5**	**20**	**20**	**0.063**
10	**5**	**25**	**25**	**0.040**
10	**5**	**30**	**30**	**0.028**

Figure 10 shows the schematic process flow for fabricating the structures consisting of Si nanowires on Si islands. We started with a Si (100) substrate coated with a thin SiO_2 film. After the SiO_2 film was patterned by photolithography and wet etching, the sample was etched by KOH. The anisotropic etch by KOH formed Si islands with four Si (111) sidewalls, each of which formed a 54.7 ^{o} angle with the bottom Si (100) surface. The SiO_2 was removed by HF afterwards. An SEM image of the fabricated Si islands was shown in Figure 11a. Au nanoclusters were deposited onto the exposed Si surfaces in an aqueous solution of HF and $KAuCl_4$. The concentrations of HF and $KAuCl_4$ were 0.2M and 0.01M, respectively. The deposition time was 30 seconds. Si nanowires were grown by a chemical vapor deposition

process [37, 38]. Silicon tetrachloride ($SiCl_4$, Aldrich, 99.99%) was used as the precursor. Hydrogen gas (10% in argon by volume) was used as the carrier gas. The nanowires were grown at 850 ℃ via a vapor-liquid-solid mechanism [37]. The Si nanowires synthesized by this method had a strong preferred growth direction along the <111> axis, and therefore were vertical to the exposed Si (111) sidewalls. An SEM image taken after the growth of Si nanowires was shown in Figure 11b. The Au clusters at the tips of the nanowires were removed by an aqueous solution of HCl and HNO_3 (aqua regia), followed by treatment with HF. The sample was thoroughly rinsed in deionized water and dried in air before the contact angle was measured.

All the SEM images were taken by a Philips XL-30 field emission SEM setup. The Lotus leaf was purchased from a local Chinese grocery store. The leaf was dried and coated with a ~3 nm thin gold film by sputtering before the SEM images were taken.

The static water contact angles were measured according to the sessile droplet method using a drop shape analysis system (AST Products, Inc.) with a computer-controlled liquid dispensing system. Water droplets with a volume of 8 μl were used. The experiment was performed under normal laboratory ambient conditions, 20 ℃ and 40% relative humidity. The contact angles were measured five times on each sample.

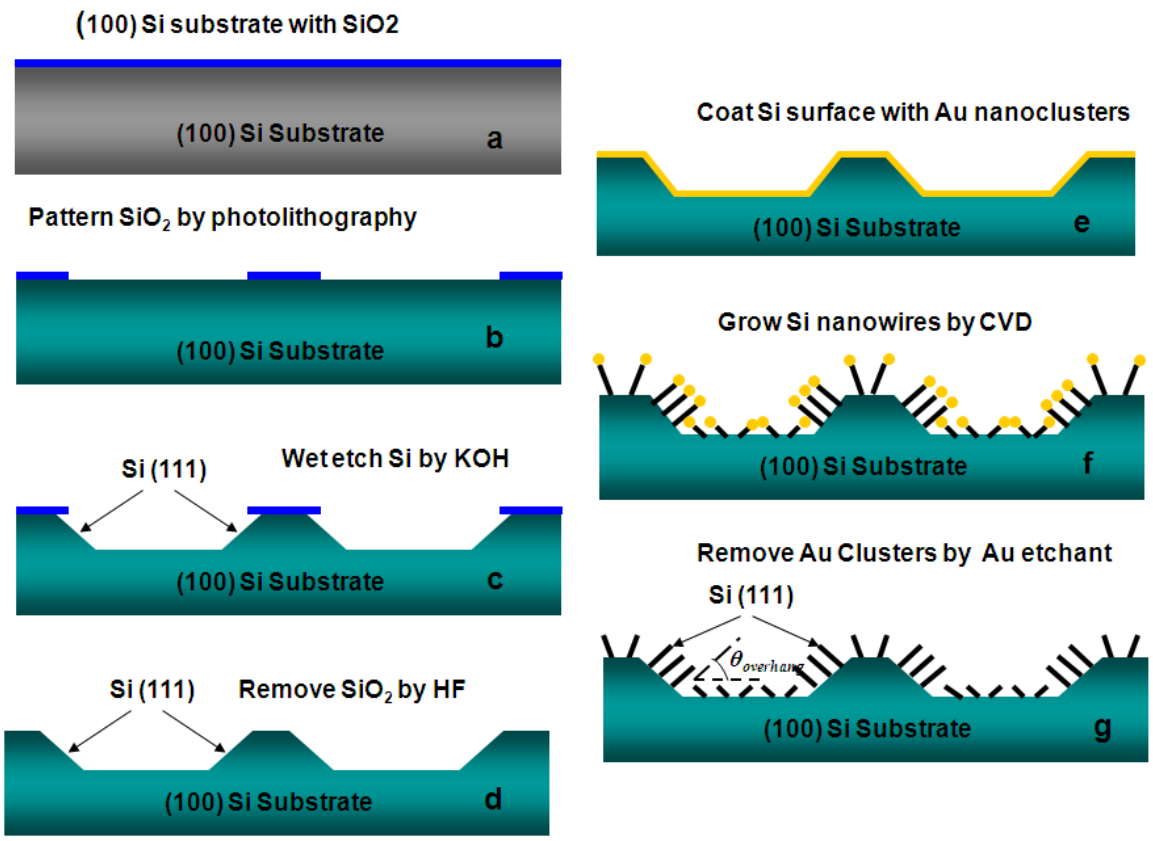

Figure 10. Schematic process flow to fabricate the structures consisting of Si nanowires on Si islands.

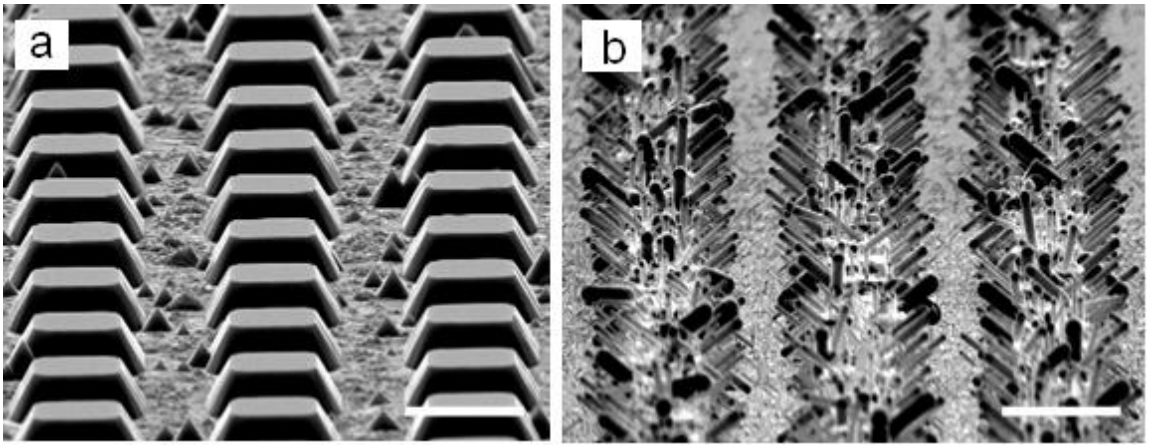

Figure 11. SEM images. (a) Si islands fabricated by etching a SiO_2-masked Si(100) substrate in KOH. (b) Si nanowires grown on the Si islands with Au clusters on the tips of the nanowires. The scale bars are 5 μm.

3.1.2 Results and discussion

The micrometer-sized Si pillars with overhangs at the top edges fabricated by micromachining techniques are shown in Figs. 12a and b. The top surfaces of the Si pillars were 5 μm × 5 μm squares, and 15 μm above the bottom surfaces. The overhanging Si (111) sidewalls formed an angle ($\theta_{overhang}$) of 54.7 ° with the top Si (100) surfaces. We fabricated a series of such Si pillar arrays by varying the center-to-center distance (x) between adjacent pillars from 13 to 50 μm. The θ_{flat} of H-terminated Si surface was measured to be 74 ± 3 °, which was consistent with previous reports [39]. Therefore, these Si pillars provide us with an ideal system to study the wettability of surfaces consisting of overhanging structures with $\theta_{overhang} < \theta_{flat} < 90$ °.

The static water contact angles of these surfaces were measured (Fig. 12c), and plotted as a function of ϕ_s in Figure 12d. It was observed that θ_{rough} increased from ~139 ° to ~162 ° as ϕ_s decreased from ~ 0.15 to ~ 0.04 until x reached ~ 30 μm. When x was further increased, the measured contact angles were scattered and unrepeatable, owing to the tendency of drops to fall in the texture for such large gaps. When x was less than 30 μm, the relationship between θ_{rough} and ϕ_s agrees well with the Cassie-Baxter equation.

The fabricated surfaces with overhang structures by growing Si nanowires on micromachined Si islands are shown in Figure 13a. The top surfaces of the Si islands were 5 μm × 5 μm squares, with a 15 μm center-to-center distance. The height of the islands was ~ 8 μm. The Si (111) sidewall of the islands formed a 54.7 ° angle with the bottom Si (100) surface. The Si nanowires were ~ 3 μm long with varied width ranging from 100 to 500 nm. The Si nanowires grown vertically on the sidewalls of two adjacent Si islands faced each other, and formed an overhanging structure with a $\theta_{overhang}$ of 35.3 ° (Fig. 13b). The hierarchical structures

consisting of Si nanowires on Si islands provide another model system that satisfies the condition of $\theta_{overhang} < \theta_{flat} < 90°$. The static water contact angle on the surface shown in Figure 13a was measured to be ~ 160 º.

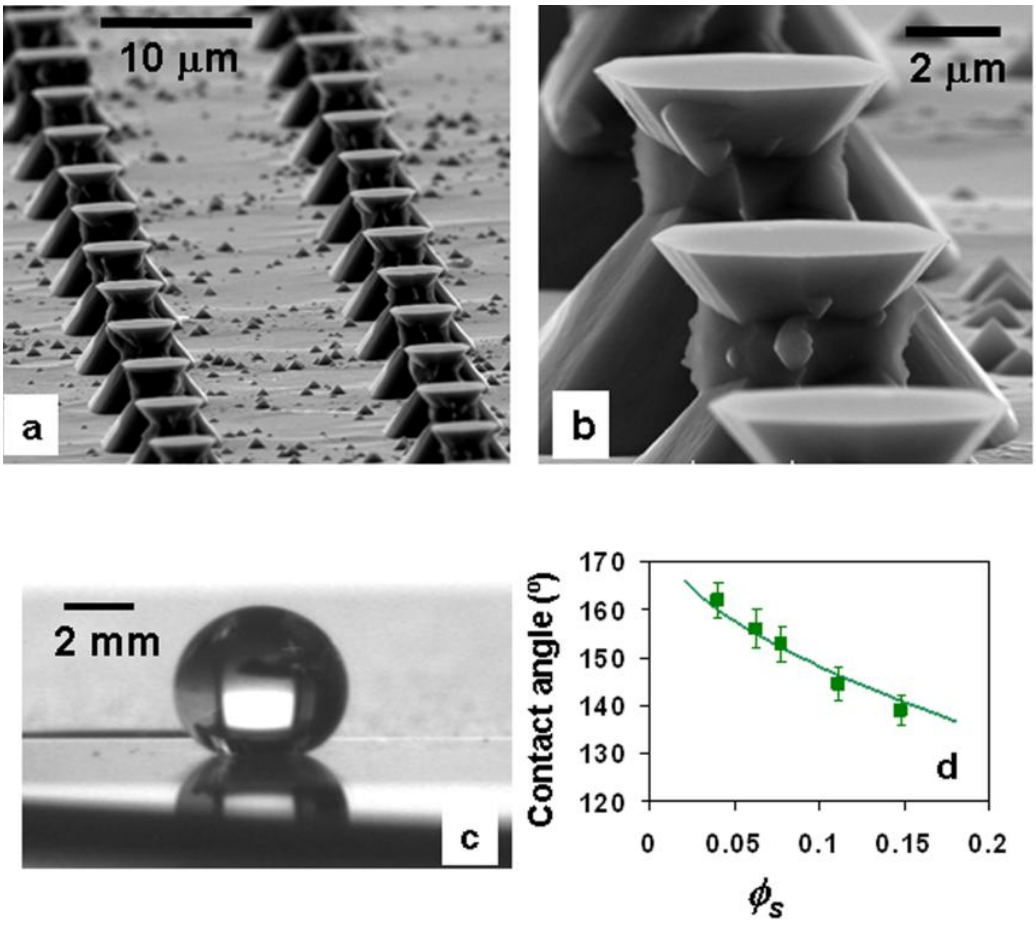

Figure 12. Superhydrophobic surfaces consisting of Si pillars with overhangs at the top edges. (a) SEM image of the Si pillars. (b) A close-up SEM image of (a). (c) An optical image of a water droplet on the Si pillars during the contact angle measurement. (d) Static water contact angles measured as a function of ϕ_s. The solid line is plotted according to the Cassie-Baxter relation (Eqn. 4).

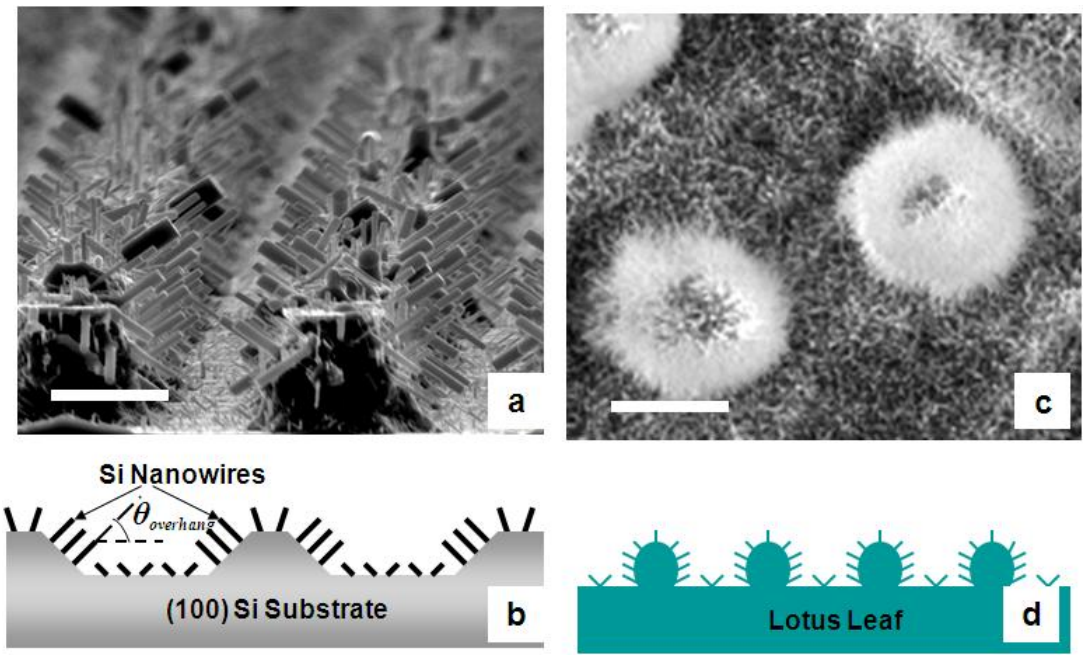

Figure 13. Superhydrophobic surfaces with hierarchical structures. (a) SEM image of Si nanowire arrays grown on micrometer-sized Si islands. (b) A schematic cross-sectional profile of (a). (c) SEM image of the surface of a Lotus leaf. (d) A schematic cross-sectional profile of (c). The scale bars in (a) and (c) are 5 μm.

Superhydrophobicity has been observed on plant leaves where hydrophobic wax is absent [29]. Recent experiments have also found that θ_{flat} of the wax on the superhydrophobic surfaces of Lotus leaves is approximately 74 º, which is in contrary to the expected values of greater than 90 º [30]. These observations cannot be understood by the previous explanation of the "Lotus effect", *i.e.*, a wax-induced hydrophobicity ($\theta_{flat} > 90°$) enhanced by the surface roughness. The results obtained in our experiments provide a plausible explanation to these phenomena. The

hierarchical structures on the surface of Lotus leaves consist of microscale bumps and nanoscale hair-like protrusions (Fig. 13c). They form a similar surface topography (Fig. 13d) as the surfaces constructed using Si nanowires and Si islands. The θ_{flat} of the carnauba wax on the surface of Lotus leaves is approximately 74°, which is also similar to the θ_{flat} of the H-terminated Si surface. Therefore, the superhydrophobicity of these Lotus leaves may be induced by the same mechanism that has been suggested to explain the superhydrophobicity of the hierarchical Si nanowire structures – the overhanging structures formed by the nanometer-sized protrusions cause water to contact a composite surface of solid and air in a metastable Cassie state, resulting in an apparent superhydrophobicity on surfaces with a θ_{flat} of less than 90°.

Following the similar principle, Tuteja *et al.* demonstrated the possibility of designing superoleophobic surfaces using intrinsically oleophilic materials with "re-entrant surface curvatures" (Fig. 14) [40]. The balance between the external pressure and the capillary force was used to evaluate the robustness of the metastable Cassie state, where the characteristic capillary rise height can be calculated from $h = \frac{2\gamma_{lv}\cos\theta}{\rho g D}$, which is inversely proportional to the cavity size *D*. It was demonstrated that the presence of special topographic structures (*e.g.*, re-entrant curvature or overhangs) is not a sufficient condition for developing highly nonwetting surfaces, because the metastable Cassie state may be inaccessible in practice if the capillary force that prevents the liquid from entering the air pocket can be easily overcome, in which case the Cassie state transits into the Wenzel state. This analysis may help us understand our experimental result that the superhydrophobic behavior becomes unstable when *x* in our silicon pillar design is beyond ~30 μm (Fig. 12).

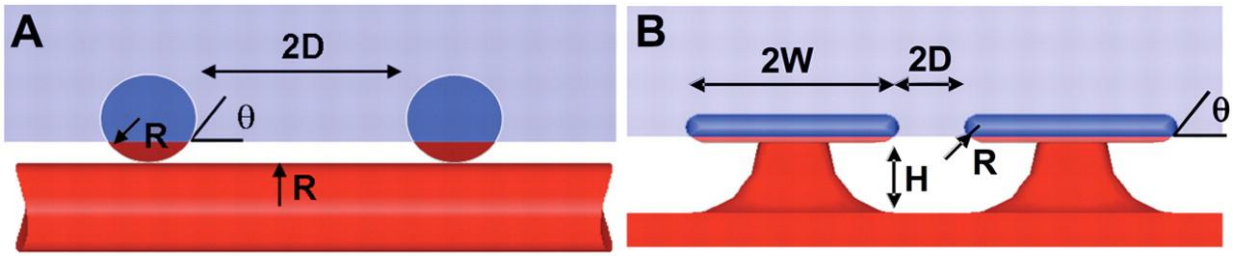

Figure 14. Schematics of re-entrant surface curvatures for the electrospun fibers (A) and the micro-hoodoos (B). The blue surface is wetted while the red surface remains nonwetted when in contact with a liquid whose equilibrium contact angle (intrinsic contact angle) is θ ($< 90°$) [40].

3.1.3 Conclusion

In summary, we have fabricated micro-textures consisting of overhanging structures of Si with well-defined geometries in both micrometer and nanometer scales. Although the intrinsic water contact angle of the H-terminated Si surface is about 74°, the constructed surfaces induce superhydrophobic behavior. Certainly, problems such as the quantitative evaluation of the stability of the metastable Cassie state, the hydraulic pressure required to wet the surfaces fabricated in our work, and the transition between the Cassie and the Wenzel states in terms of contact angle hysteresis still need to be studied further. Nonetheless, it is expected that this work could provide additional insight into the interesting superhydrophobic phenomena found in nature and that the principle could be applied to make intrinsically hydrophilic materials superhydrophobic by tailoring the surface topography.

3.2 FABRICATION OF NON-AGING SUPERHYDROPHOBIC SURFACES BY PACKING FLOWER-LIKE HEMATITE PARTICLES

In this section, we report the fabrication of superhydrophobic surfaces by packing flower-like particles of hematite (α-Fe_2O_3), an intrinsically hydrophilic material. These superhydrophobic surfaces do not age even in extremely oxidative environments—they are able to retain the superhydrophobicity after being stored in ambient laboratory air for 4 months, heated to 800 ℃ in air for 10 hours, and exposed to ultraviolet ozone for 10 hours.

3.2.1 Experimental design and methodology

The flower-like α-Fe_2O_3 particles were synthesized by using an ethylene glycol (EG)-mediated reaction. The synthesis process was adopted from Zhong *et al.* [41] with the following modifications: (i) the surfactant was removed from the previously used reaction system, and (ii) iron nitrate [$Fe(NO_3)_3$] was used to replace the previously used iron chloride. In a typical synthesis process, 0.7 g $Fe(NO_3)_3$ (Fisher Scientific) and 0.7 g urea ($CO(NH_2)_2$, Sigmar-Aldrich) were added into 60 mL ethylene glycol ($C_2H_6O_2$, J.T. Baker) to form a cloudy mixture. The mixture was then stirred with a magnetic stirrer bar and heated to 170 ℃. The cloudy mixture turned clear in 10 min and became opaque again after 20 min, indicating the formation of iron oxide precursor. The products were collected by centrifugation–redispersion cycles with alcohol. The collected products were then calcined in air at 450 ℃ for 3 hours in a tube furnace (Lindberg) to obtain α-Fe_2O_3 particles. The α-Fe_2O_3 particles were characterized by X-ray diffractometry (XRD, Philips X'pert), transmission electron microscopy (TEM, JEOL 2000FX), and scanning electron microscopy (SEM, Philips XL-30).

We fabricated superhydrophobic surfaces by packing these particles through three approaches: (i) particles were dispersed in ethanol, and the mixture was drop-cast onto a double-sided tape adhered to a glass slide, followed by baking in air at 80℃ for an hour; (ii) a multipurpose glue (3M) was first sprayed on a piece of stainless steel, then the particles (dispersed in ethanol) were sprayed onto the glue using an airbrush (Iwata), followed by baking in air at 80℃ for an hour; and (iii) the particles were compressed into a tablet using a pellet die (Sigma Aldrich).

The water contact angle (WCA) was measured using a VCA-OPTIMA drop shape analysis system (AST Products, Inc.) with a computer-controlled liquid dispensing system and a motorized tilting stage. Water droplets with a volume of 4 μl were used to measure the static WCA. The advancing and receding angles were recorded during expansion and contraction of the droplets induced by placing a needle in the water droplets and continuously supplying and withdrawing water through the needle. The sliding angle was measured by tilting the stage and recorded when the droplet began to move in the downhill direction. The experiments were performed under normal laboratory ambient conditions (20 ℃ and 40% relative humidity). The WCA was measured five times on each sample.

3.2.2 Results and discussion

The SEM and transmission electron microscopy (TEM) images of the synthesized particles were shown in Figs. 15a and b, respectively. These particles are spheres of 1-2 μm in diameter. They have a rough surface consisting of 40-60 nm thick distorted plates, which resemble the shape of petals of a flower. Figure 15c shows a TEM image taken at the edge of a plate on the surface of the particle. It is seen that the thin plate is composed of interconnected crystals of about 5 nm in

diameter. Figure 15d shows the X-ray diffraction (XRD) pattern of the synthesized particles, indicating that the particles consist of crystalline Fe_2O_3 with a rhombohedral symmetry.

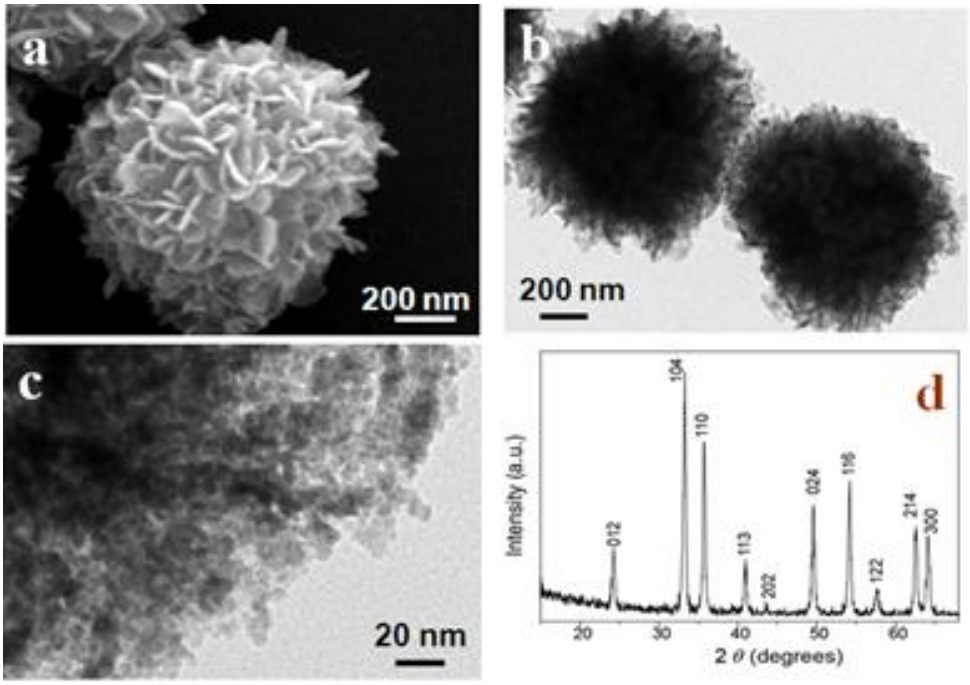

Figure 15. Flower-like α-Fe_2O_3 particles. (a) An SEM image of a particle. (b) A TEM image of two α-Fe2O3 particles. (c) TEM image taken at the edge of a plate. (d) XRD pattern of the synthesized particles.

Figure 16a showed a typical SEM image of the surfaces made by packing the flower-like α-Fe_2O_3 particles. It was observed that the particles retained their flower-like morphology after they were packed by any of the above three approaches. The topography of these surfaces consisted of structures in multiple length scales—the roughness caused by the thin plates, or "petals", on each particle was superimposed onto a larger scale roughness formed by packing the particles. Figure 16b showed a 4 μl water droplet on the surface with a WCA of 159 ± 2°, which moved around rapidly when it was slightly disturbed, and dripped off the substrate rapidly when

the substrate was tilted less than 2 °. Despite the differences in the sample preparation methods, a static WCA of greater than 150 ° and a hysteresis—the difference between the advancing and receding WCA—of less than 3 °were consistently obtained.

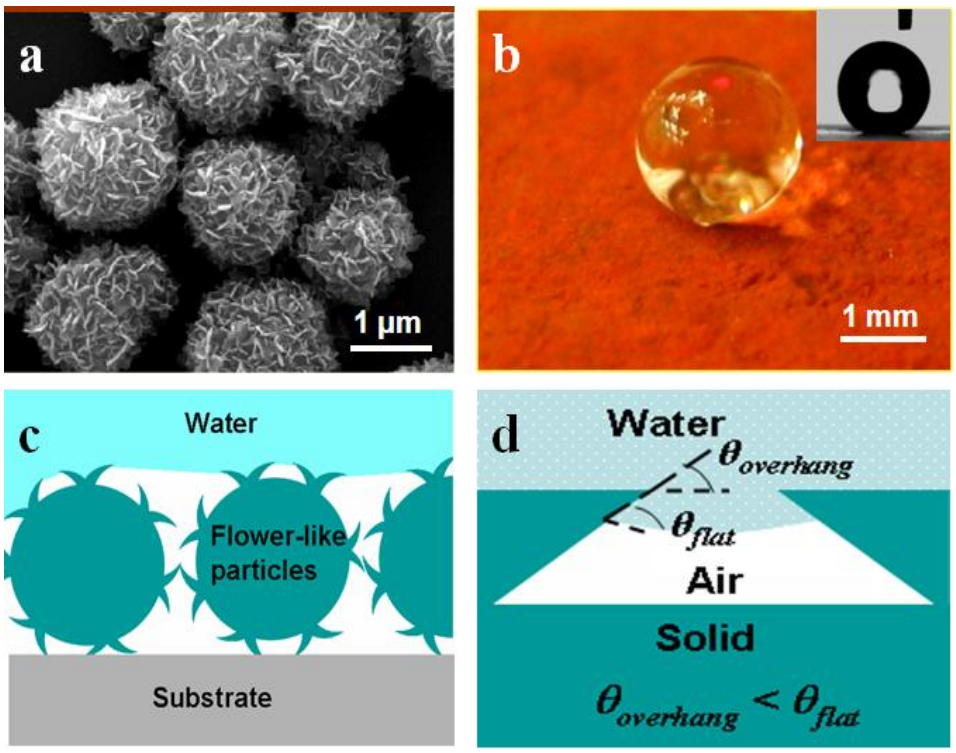

Figure 16. Superhydrophobic surfaces fabricated by packing the flower-like α-Fe2O3 particles. (a) A typical SEM image of the surfaces. (b) Optical image of a water droplet on the surface. Inset is an optical image of the water droplet during the WCA measurement. (c) Schematic cross-sectional profile of water in contact with the flower-like particles. (d) Schematic cross-sectional profile of water in contact with a solid indent consisting of overhanging structures.

α-Fe_2O_3 is an intrinsically hydrophilic material [42]. Heating the samples in a tube furnace (Lindberg) to 800 ℃ in air and exposing them to ultraviolet ozone (UVO Jelight Inc.) for

10 hours are sufficient to remove the possible organic residuals left on the surface of the particles after the synthesis process. Therefore, the observed superhydrophobic phenomenon is induced on an intrinsically hydrophilic material. Figure 16c schematically illustrates a possible cross-sectional profile of water in contact with the flower-like particles. The distorted plates, or "petals", of the particles form overhanging structures on the surface, which prevent water from penetrating the textures and replacing the air trapped inside. A more detailed profile for water in contact with a solid indent consisting of overhanging structures is shown in Figure 16d.

According to Eqn. 4, provided that θ_{flat} for α-Fe_2O_3 is estimated to be 45 ° [42], ϕ_s needs to be less than 0.59 to make θ_{rough} greater than 90 °. This condition can be easily satisfied by the surfaces shown in Figure 16a with a schematic cross-sectional profile shown in Figure 16c. In addition, the indentation produced by the overhanging "petals" of the particles bears larger indentations on a larger scale produced by packing these particles. For surfaces with such hierarchical structures, θ_{rough} increases monotonically as the generation of the indentation hierarchy increases. Therefore, the hierarchical topography of the surfaces consisting of these flower-like particles further increases θ_{rough} to over 150 ° and induces the observed superhydrophobic phenomenon.

To prove the important role of the flower-like morphology of the synthesized Fe_2O_3 particles for inducing the superhydrophobic behavior, we mechanically ground the particles using an agate mortar to destroy their flower-like morphology (Fig. 17a) and repeated the experiment. We found that surfaces made by packing these ground particles were hydrophilic with static WCAs of less than 20 °and sliding angles of greater than 90 °, which was in an obvious contrast to the results obtained from these particles before they were ground. We also made surfaces by packing commercial Fe_2O_3 particles in two different sizes (2 μm in Fig. 17b and 50

nm in Fig. 17c in diameter, respectively, purchased from Sigma Aldrich) that did not have the flower-like morphology, and found that the samples made using these particles were also hydrophilic. The results of the WCA measurements are summarized in Table 3.

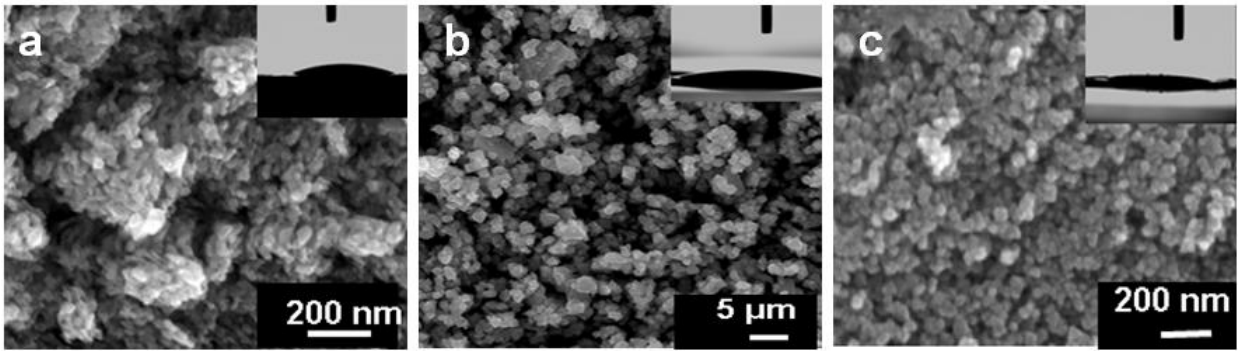

Figure 17. SEM images of (a) mechanically ground particles, (b) commercial micrometer-sized particles, and (c) commercial nanometer-sized particles. Insets are the optical images of the water droplet during the WCA measurement.

α-Fe_2O_3 is one of the most stable metal oxides in nature [42]. We therefore anticipate that the fabricated surfaces consisting of the flower-like α-Fe_2O_3 particles can not be further oxidized, and the superhydrophobicity of the surfaces can be preserved for a long time in laboratory ambient conditions. Indeed, these surfaces retained their superhydrophobicity after being stored in ambient laboratory air (20 ℃ and 40% relative humidity) for 4 months. We further carried out ageing tests by placing these samples in extremely oxidative environments—they were heated to 800 ℃ in air for 10 hours, and exposed to ultra-violet ozone (UVO) for 10 hours. No significant changes in the WCAs or hysteresis were observed after these treatments (Table 3).

Table 3. Results of WCA measurements on surfaces made by packing α-Fe_2O_3 particles with different morphologies before and after ageing treatments.

Hematite particles*		WCA measured on fresh sample ( )	WCA measured after ageing treatments ( )		
			Stored in ambient laboratory air for 4 months	Heated in air at 800 °C for 10 hours	Exposed to UVO for 10 hours
Synthesized flower-like particles	Static WCA	159 ±2	157 ±2	158 ±2	157 ±2
	Hysteresis	~ 2	~ 2	~ 2	~ 2
	Sliding angle	< 2	< 2	< 2	< 2
Synthesized particles after they were mechanically ground into irregular shapes	Static WCA	17 ±3	16 ±3	17 ±3	17 ±3
	Sliding angle	>90	>90	>90	>90
Commercial particles of 2 µm in average diameter	Static WCA	13 ±3	12 ±3	15 ±3	12 ±3
	Sliding angle	>90	>90	>90	>90
Commercial particles of 50 nm in average diameter	Static WCA	<10	<10	<10	<10
	Sliding angle	>90	>90	>90	>90

*All the samples are made by compressing particles into a tablet using a pellet die to remove the effect of any possible organic contaminations from the adhesion layer that is needed when other approaches are used to pack the particles on the substrate.

3.2.3 Conclusion

In this work, it is evident that the flower-like morphology of the synthesized Fe_2O_3 particles—micrometer-sized spheres with nanometer-sized protrusions—is essential for making the surfaces consisting of these particles superhydrophobic. Such superhydrophobicity is induced by the overhang structures present on the surface and does not require the material to be intrinsically hydrophobic. After the ageing tests, because the α-Fe_2O_3 particles retain their flower-like morphology (as confirmed by SEM and TEM characterizations), the superhydrophobicity of the surfaces made by packing these particles is preserved. Because a variety of flower-like structures have been synthesized and reported in the literatures [43-45], we anticipate that the demonstrated approach of packing flower-like structures could also be applied to many other materials for fabrication of non-ageing superhydrophobic surfaces. Such surfaces may provide a solution to the ageing and decay problems that currently hinder the practical applications of artificial superhydrophobic surfaces.

3.3 SUPER WATER AND OIL-REPELLENT SURFACES ON INTRINSICALLY HYDROPHILIC AND OLEOPHILIC POROUS SILICON FILMS

In this section, we report a convenient approach to fabricate porous Si films that are able to induce a superoleophobic behavior on intrinsically oleophilic surfaces. The porous Si films are fabricated by a gold-assisted electroless etching process, which produces a hierarchical porous structure that consists of micrometer-sized asperities superimposed onto a network of tilted nanometer-sized pores. The hierarchical porous structure forms textures with overhanging

structures on the surface, which are able to induce a superhydrophobic behavior on the intrinsically hydrophilic Si surface. After chemically modified with a self-assembled monolayer (SAM) of fluorinated organic molecules, which provides a lower surface free energy, the porous Si films become super oil-repellent to diethylene glycol and hexadecane with θ_{rough} of greater than 150 º, although the coated Si surface is intrinsically oleophilic with θ_{flat} of less than 90 º for these oils. It is speculated that this superoleophobic phenomenon is induced by the overhang structures present on the surface following the same mechanism that induces the superhydrophobic phenomenon on intrinsically hydrophilic materials.

3.3.1 Experimental design and methodology

Two types of porous Si films were prepared in our experiment—one has tilted pores, and the other has vertically aligned straight pores. The first type of porous Si was prepared by gold (Au)-assisted electrochemical etching process. In this process, a p-type Si (111) wafer (Boron-doped, 1-10 Ω·cm) purchased from Silicon Quest International, Inc. was used. It was diced to 1 cm × 1 cm chips for the experiment. The Si surface was first coated with Au nanoclusters, which served as the electrochemical reaction center during the etching step. The Au coating solution was made by dissolving 0.01 M $KAuCl_4$ (99.995%, Aldrich) in 10 % HF aqueous solution (EMD). The Si chips were dipped in the coating solution at room temperature for 30 seconds, and then were soaked in an etching solution at 50^{o}C for a variety of periods. The etching solution was made by dissolving 0.135 M $Fe(NO_3)_3$ (Fisher Scientific) in 10% HF aqueous solution. After the etching process, the samples were rinsed by ethanol, deionized water and dried by nitrogen gas.

The second type of porous Si with the vertically aligned straight pores was prepared by anodic etching of Si (100) chips. A p-type silicon (100) wafer (Boron-doped, <1mΩ·cm) was purchased from Siltronix (France), and diced into 2 cm × 2 cm chips. A Teflon electrochemical cell that exposed 1.6 cm^2 of the Si chip was employed for the anodic etching process. The etching solution consisted of 3:1 (v/v), 48% aqueous HF–ethanol solution. A direct current at a density of 100 mA/cm^2 was applied for 10 min. After the etching process, the samples were rinsed by ethanol, deionized water and dried by nitrogen gas.

Prior to the SAM coating process, the samples were firstly exposed to ultraviolet ozone (UVO) (Jelight Inc.) for 15 min at room temperature to oxidize the Si surface. The samples were then immersed into the SAM coating solution, made by dissolving 0.5 mM (tridecafluoro-1,1,2,2,-tetrahydrooctyl) trichlorosilane (FTS) ($n\text{-}C_6F_{13}CH_2CH_2SiCl_3$, Gelest Inc.) into a 4:1 (v/v) mixture of hexadecane (anhydrous, Sigma-Aldrich) and chloroform (anhydrous, Sigma-Aldrich). After ~15 minutes, the samples were sequentially rinsed with isooctane (Sigma-Aldrich), isopropanol (Fisher Scientific), deionized water, and then dried by nitrogen gas.

Scanning electron microscopy (SEM) images were taken by a Philips XL-30 field-emission SEMsetup. The contact angle was measured using a VCA-OPTIMA drop shape analysis system (AST Products, Inc.) with a computer-controlled liquid dispensing system and a motorized tilting stage. Droplets of liquids in a volume of 5 μL were used to measure the static contact angle. The advancing and receding angles were recorded during the expansion and contraction of the droplets induced by placing a needle in the water droplets and continuously supplying and withdrawing water through the needle. The sliding angle was measured by tilting the stage and recorded when the droplet began to move in the downhill direction. The experiments were performed under normal laboratory ambient conditions (20 ℃ and 40%

relative humidity). Each contact angle measurement was repeated three times at different places on the sample, and the mean value was reported.

3.3.2 Results and discussion

Au-assisted electroless etching processes have been previously employed to prepare Si nanowires and porous Si films [46]. The process is applied here to make hierarchical porous structures on Si surfaces. Au clusters were first deposited onto the Si surface via a galvanic displacement reaction mechanism, by dipping the Si chip in an aqueous solution containing $KAuCl_4$ and HF. The chip was then transferred to an etching solution containing $Fe(NO)_3$ and HF, where pores were formed by oxidizing Si while reducing Fe^{3+}. The Au clusters coated onto the Si prior to the etching step are believed to act as the local electrodes that attract electrons from the Si underneath and facilitate Si oxidation and dissolution during the etching process, as shown in Figure 18. Therefore, pores are formed where the Au clusters are present, and the Au clusters sink into the pores as the etching proceeds.

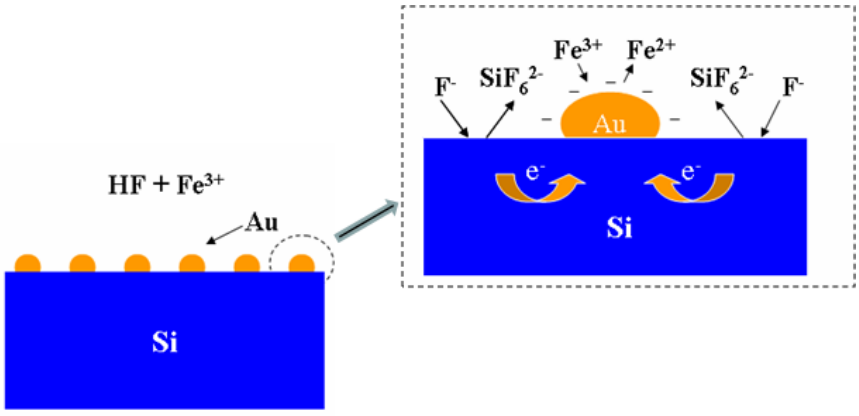

Figure 18. Schematic of Au-assisted electroless etching

Since the etching prefers to proceed along the Si <100> direction, on a (111) Si surface, tilted pores are formed. Figs. 19a and b show the representative top and cross-sectional SEM images of the as-fabricated porous silicon films after 1 hour etching. A network of tilted pores in nanometer scales is clearly seen in these images. In addition, asperities in the micrometer scale are observed, and the topography of the asperities is superimposed onto the network of nanometer pores.

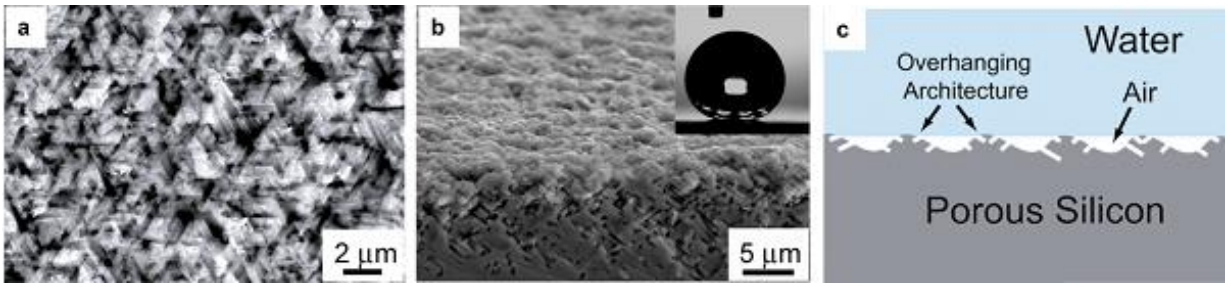

Figure 19. Porous silicon surface fabricated by Au-assisted electroless etching. (a) Top-view SEM image. (b) Cross-sectional view SEM image. The inset is an optical image of a water droplet on the surface. (c) Schematic cross-sectional profile of water in contact with the porous silicon surface.

The as-fabricated sample was superhydrophobic. The static water contact angle was measured to be ~160 º (Fig. 19b inset). The hysteresis—the difference between the advancing and receding angle—was measured to be less than 2 º, and water droplets (~ 5 μl) roll off the substrate at a sliding angle of less than 2 º. Because no organic chemicals are involved in the entire fabrication process to further decrease the surface free energy, we attribute the observed superhydrophobic phenomenon on the intrinsically hydrophilic Si surface to the hierarchical topographic characteristic of the porous Si.

As schematically shown in Figure 19c, the superimposition of the micrometer-scale asperities onto the network of nanometer pores forms overhang structures, which may induce the observed superhydrophobic phenomenon on the intrinsically hydrophilic Si surface. Figure 20 schematically shows two possible cross-sectional profiles of liquids in contact with the as-fabricated porous silicon. Two critical parameters in these profiles are: (i) the angle ($\theta_{overhang}$) formed between the sidewalls of the indent and the horizontal line, and (ii) the intrinsic contact angle (θ_{flat}) of the substrate. When $\theta_{overhang}$ is greater than θ_{flat} (Fig. 20a), the liquid-air interface (or meniscus) inside the indent produces a capillary force that draws the liquid into the pores. As a result, the liquid is in complete contact with silicon—a state that has been referred to as Wenzel state. When $\theta_{overhang}$ is less than θ_{flat} (Fig. 20b), the liquid-air interface inside the indent produces a capillary force that is able to prevent liquid from entering the indent. Therefore, the liquid is in contact with a composite surface of solid and air—a state that has been referred to as Cassie state. When water is in contact with the freshly prepared porous Si with a H-terminated Si surface, θ_{flat} is about 80°, which is greater than $\theta_{overhang}$ as observed from the SEM image (Fig. 19). Therefore, the profile of water in contact with porous Si is represented by Figure 20b, which is in the Cassie state.

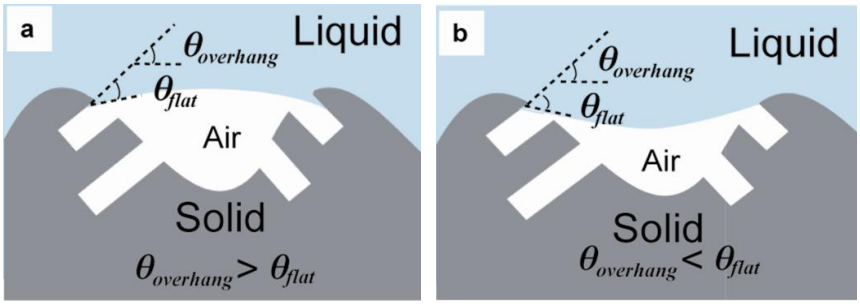

Figure 20. Schematic cross-sectional profile of liquid in contact with the porous silicon surface consisting of overhang structures in the case of (a) $\theta_{overhang} > \theta_{flat}$ and (b) $\theta_{overhang} < \theta_{flat}$.

The experiment was repeated on porous Si samples prepared by varying the etching time, which produced surfaces with varied ϕ_s. The static water contact angle (WCA) on these samples were measured and plotted in Figure 21. It was observed that the static WCA increased from ~ 102 ° to 162 ° as the etching time increased from 5 min to 40 min, while after 40 min, etching the Si for a longer time did not significantly increase the contact angle. The increase in the WCA as a function of the etching time is likely due to a decrease in ϕ_s when the Si is etched for a longer time.

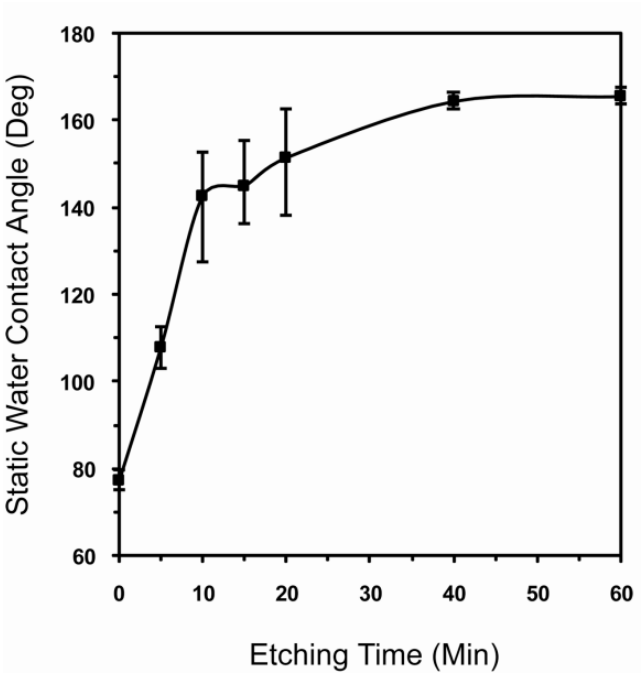

Figure 21. Static water contact angle measured on the porous Si as a function of the etching time.

To prove the important role that the surface topography plays in inducing the superhydrophobic phenomenon on the Si surface with tilted pores, porous Si with vertically aligned straight pores were fabricated by anodic etching and the wetting phenomenon on such porous Si surfaces was examined. Figure 22a shows an SEM image of the as-fabricated porous silicon by anodic etching. The nanometer-sized pores are vertically aligned along the surface normal direction of the Si chip, and no micrometer-sized asperities are present on the surface. The porous Si surfaces with straight pores exhibit hydrophilic behavior. It can be explained that, when water is in contact with such surfaces (schematically shown in Fig. 22b) without the presence of overhanging structures, the capillary force will draw water into the pores. As a result, water is in complete contact with silicon.

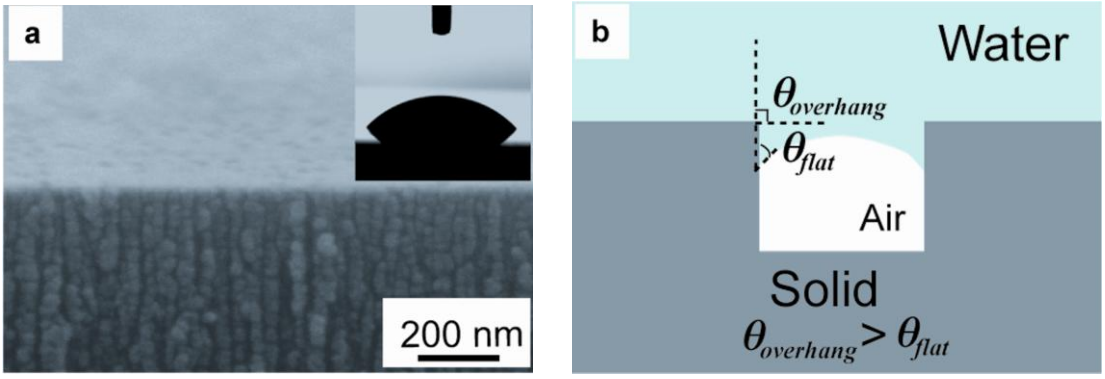

Figure 22. Water in contact with the porous Si with vertically aligned straight pores. (a) Representative SEM image of the porous silicon with vertically aligned straight pores. The inset is an optical image of a water droplet on the surface. (b) Schematic cross-sectional profile of water in contact with the porous silicon surface, where $\theta_{overhang} > \theta_{flat}$.

Intrigued by the superhydrophobic phenomenon observed on intrinsically hydrophilic porous Si films, we further investigated the wettability of oil on such porous Si surfaces with tilted pores, before and after coating them with an organic molecule. Porous Si samples prepared by 1 h etching (Fig. 19) were used. The wetting properties were evaluated using two oils: diethylene glycol and hexadecane, with surface tensions of 44.8 mN/m and 27.5 mN/m, respectively. As shown in Figure 23, before coating the sample, the porous Si surfaces are superhydrophobic but oleophilic. The contact angles of diethylene glycol and hexadecane were both measured to be less than 15 °. This result is expected, because θ_{flat} of diethylene glycol and hexadecane are ~ 40 ° and ~ 3 °, respectively, on hydrogen-terminated Si surfaces, which is smaller than $\theta_{overhang}$ of the porous Si film. As the case shown in Figure 20a, these oils are in complete contact with Si.

After coating the flat Si with a self-assembled monolayer of FTS, the θ_{flat} of water, diethylene glycol, and hexadecane on the FTS-coated Si were measured to be 109.2 °, 81.5 ° and 70.7 °, respectively. When the coating was applied to porous Si films, the coated films became super oil-repellent with θ_{rough} of greater than 150^{o} for both diethylene glycol and hexadecane (Fig. 23). This is interesting considering the fact that the FTS-coated Si is intrinsically oleophilic with θ_{flat} of less than 90 ° for both oils. We speculate that such a super oil-repellency is induced by the same mechanism that induces the superhydrophobic phenomenon on intrinsically hydrophilic porous Si films. Because θ_{flat} of oil is larger than $\theta_{overhang}$ after coating the surface with FTS, the overhang structures can prevent oil from penetrating the texture (Fig. 20b). Therefore, the oil is in contact with a composite surface of air and solid (Cassie state) and exhibits an apparent contact angle of greater than 150 °.

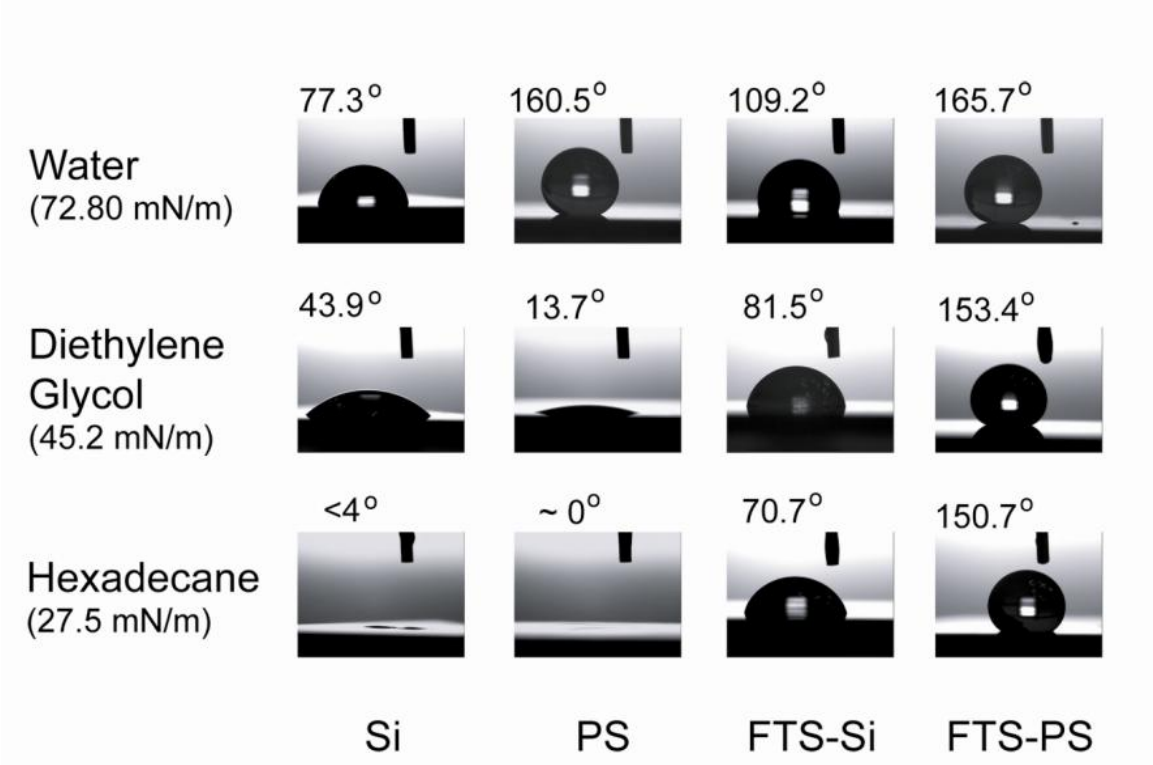

Figure 23. Static contact angles of water, diethylene glycol, and hexadecane on flat silicon (Si), porous silicon (PS), flat silicon coated with FTS (FTS-Si) and porous silicon coated with FTS (FTS-PS).

3.3.3 Conclusion

We have demonstrated a convenient approach to fabrication of porous Si films that are able to induce a superhydrophobic behavior on an intrinsically hydrophilic Si surface and a superoleophobic behavior on an intrinsically oleophilic FTS-coated Si surface. The hierarchical porous structure of the films forms overhang structures on the surface, which play an important

role in inducing the superhydrophobic and superoleophobic phenomena. Certainly, problems such as the dynamic behavior of the oils on the superoleophobic surfaces and the quantitative evaluation of the stability of the Cassie state still need further investigation. Nonetheless, it is anticipated that the demonstrated approach and principle could be applied to expand the range of materials that can be used to fabricate superhydrophobic and, in particular, superoleophobic surfaces.

3.4 TRANSPARENT SUPERHYDROPHOBIC AND HIGHLY OLEOPHOBIC COATINGS

In this section, we report a facile process for fabrication of transparent superhydrophobic and highly oleophobic surfaces through assembly of silica nanoparticles and sacrificial polystyrene nanoparticles. The silica and polystyrene nanoparticles are first deposited by a layer-by-layer assembly technique. The polystyrene nanoparticles are then removed by calcination, which leaves a porous network of silica nanoparticles. The cavities created by the sacrificial polystyrene particles form overhang structures on the surfaces. Modified with a fluorocarbon molecule, such surfaces are superhydrophobic and transparent. They also repel liquids with low surface tensions, such as hexadecane, due to the overhang structures that prevent liquids from getting into the air pockets even though the intrinsic contact angles of these liquids are less than 90 °.

It is generally recognized that the superhydrophobicity, either natural or artificial, is a result of the interplay between the surface chemical composition and the surface texture with a two-tier roughness in micrometre and nanometre scales, respectively, for each tier. Because the

surface textures with the two-tier roughness may induce significant light scattering, fabrication of transparent superhydrophobic surfaces has been a difficult task. By optimizing and manipulating surface topographies through delicate approaches, *e.g.*, by layer-by-layer assembly [47, 48], using eutectic liquids [49], and depositing silicone nanofilaments [50], several groups have successfully fabricated transparent superhydrophobic surfaces, which are promising for many applications where the substrate material needs to be rendered superhydrophobic without significantly changing its optical properties. However, these transparent superhydrophobic surfaces are vulnerable to oil contamination—they repel water but not oil, and contamination of liquids with a low surface tension such as vegetable oil can easily remove their superhydrophobicity. Therefore, to fully explore the potential applications of transparent superhydrophobic surfaces, it is desirable to make them repel not only water but also oil and liquids with a low surface tension.

Fabricating superhydrophobic surfaces that are able to repel oil in the same manner as they repel water has been challenging, because this typically requires the solid surface to possess a sufficiently low surface free energy so that its intrinsic oil contact angle is greater than 90°, which in practice has been exceptionally difficult if possible at all. Recently, it has been demonstrated that by fabricating ‘‘overhang’’ or “re-entrant” structures on the surface, the requirement on the extremely low surface free energy may be relaxed, and surfaces that are both super water-repellent and super oil-repellent have been achieved [40, 51]. However, these coatings are not transparent, and we are unaware of published work to make transparent coatings with super repellencies to both water and oil. Herein, we develop a facile process for fabrication of transparent superhydrophobic and highly oleophobic surfaces by first depositing silica

nanoparticles and sacrificial polystyrene nanoparticles through a layer-by-layer assembly technique, and then remove the sacrificial polystyrene particles by calcination.

3.4.1 Experimental design and methodology

Materials. Poly(sodium 4-styrenesulfonate) (PSS, Mw=70,000), poly(diallyldimethylammonium chloride) (PDDA, 20 w.t.%), TM-40 colloidal silica (40 w.t.% suspension in water, ca. 20 nm diameter silica particles), chloroform (anhydrous), hexadecane (anhydrous) and isooctane were obtained from Sigma-Aldrich. Negatively charged polystyrene nanoparticles (8 w.t.% solid, 60 nm in diameter) were obtained from Interfacial Dynamics Corp. Isopropanol was obtained from Fisher Scientific. (Tridecafluoro-1,1,2,2-tetrahydrooctyl) trichlorosilane (n-C6F13CH2CH2SiCl3, abbreviated as FTS, >95%) was purchased from Gelest Inc. De-ionized (DI) water was prepared using the Milli-Q (Millipore) system.

Substrate preparation. Before the coating process, the substrates were cleaned by immersion in piranha solution (3:1 mixture of 98 w.t.% H_2SO_4 and 30 w.t.% H_2O_2; piranha solutions may result in explosion or skin burns if not handled with extreme caution) for 15min, thoroughly rinsed with DI water, and dried with a nitrogen flow. This process rendered the freshly cleaned substrates negatively charged in solution.

Layer-by-layer assembly of nanoparticles. During the assembly, the substrates were repetitively immersed into cationic and anionic aqueous solutions. In each cycle, the substrates were first immersed into cationic solutions, followed by rinsing with DI water and drying with a nitrogen flow. Then, the substrates were immersed into anionic solutions, followed by the same

rinsing and drying steps. One bilayer was formed upon completion of each cycle. The assembly process started with deposition of five bilayers of PDDA and PSS, $[PDDA/PSS]_5$, before deposition of nanoparticles. A few bilayers of polymers, such as $[PDDA/PSS]_5$, have been shown to promote the adhesion of the film to the substrate during the subsequent layer-by-layer assembly of nanoparticles [47,48]. For deposition of $[PDDA/PSS]_5$, PDDA was used to make the cationic aqueous solution (2 mg mL^{-1}, pH 4), and PSS was used to make the anionic aqueous solution (2 mg mL^{-1}, pH 4). After five bilayers of PDDA and PSS were deposited, deposition of body layers started by switching the anionic solution from the PSS solution to an aqueous solution (pH 9.0) containing two kinds of nanoparticles with different sizes (60 nm polystyrene + 20 nm SiO2, ca. 0.04 wt% each), while the PDDA aqueous solution was still used as the cationic solution. To investigate the effect of the number of the body bilayers on the wettability, samples with 5, 10, 15, 20 and 25 bilayers of nanoparticles, $[PDDA/(60\text{ nm polystyrene} + 20\text{ nm } SiO_2)]_x$ (where x denotes the number of body bilayers), respectively, were prepared. For each coating of $[PDDA/(60\text{ nm polystyrene} + 20\text{ nm } SiO_2)]_x$, two sets of samples were prepared and compared. One set was used without removing the polystyrene particles while the other set was calcined as described below to remove the polystyrene particles before it was functionalized with FTS.

Calcination of the coatings. One set of the $[PDDA/(60\text{ nm polystyrene} + 20\text{ nm } SiO_2)]_x$ samples was calcined at 550 ℃ for 4 h, during which both the polystyrene particles and polyelectrolytes were removed from the coatings and a nanoporous network of silica nanoparticles was formed.

Surface functionalization of the coatings. Both sets of the [PDDA/(60 nm polystyrene + 20 nm SiO2)]x samples were finally functionalized with FTS. The samples, either directly after layer-

by-layer assembly or after calcination, were treated with ultraviolet ozone (UVO) (Jelight Inc.) for 5 min. Then, they were immersed into a coating solution, made by dissolving 0.5 mM FTS into a 4:1 (v/v) mixture of hexadecane and chloroform. After 15 min, the samples were thoroughly rinsed by isooctane, isopropanol, and DI water, sequentially.

Characterization. The contact angle was measured using a VCA-OPTIMA drop shape analysis system (AST Products, Inc.) with a computer-controlled liquid dispensing system. Droplets of liquids in a volume of 5 ml were used to measure the static contact angle. The advancing and receding angles were recorded during expansion and contraction of the droplets induced by placing a needle in the liquid droplets and continuously dispensing and withdrawing liquid through the needle. All of the tests were performed under normal laboratory ambient conditions (20 ℃ and 40% relative humidity). Each contact angle measurement was repeated three times at different places of the sample, and the average value was reported. Scanning electron microscopy (SEM) images were taken by a Philips XL-30 field emission SEM setup. Transmittance was measured by a UV-Vis-NIR microspectrophotometer (Craic QDI 2010).

3.4.2 Results and discussion

The process for preparing the coatings is schematically shown in Figure 24 and detailed in the experimental section. It mainly consists of two steps: (i) layer-by-layer assembly of silica nanoparticles and sacrificial polystyrene nanoparticles and (ii) removal of sacrificial polystyrene

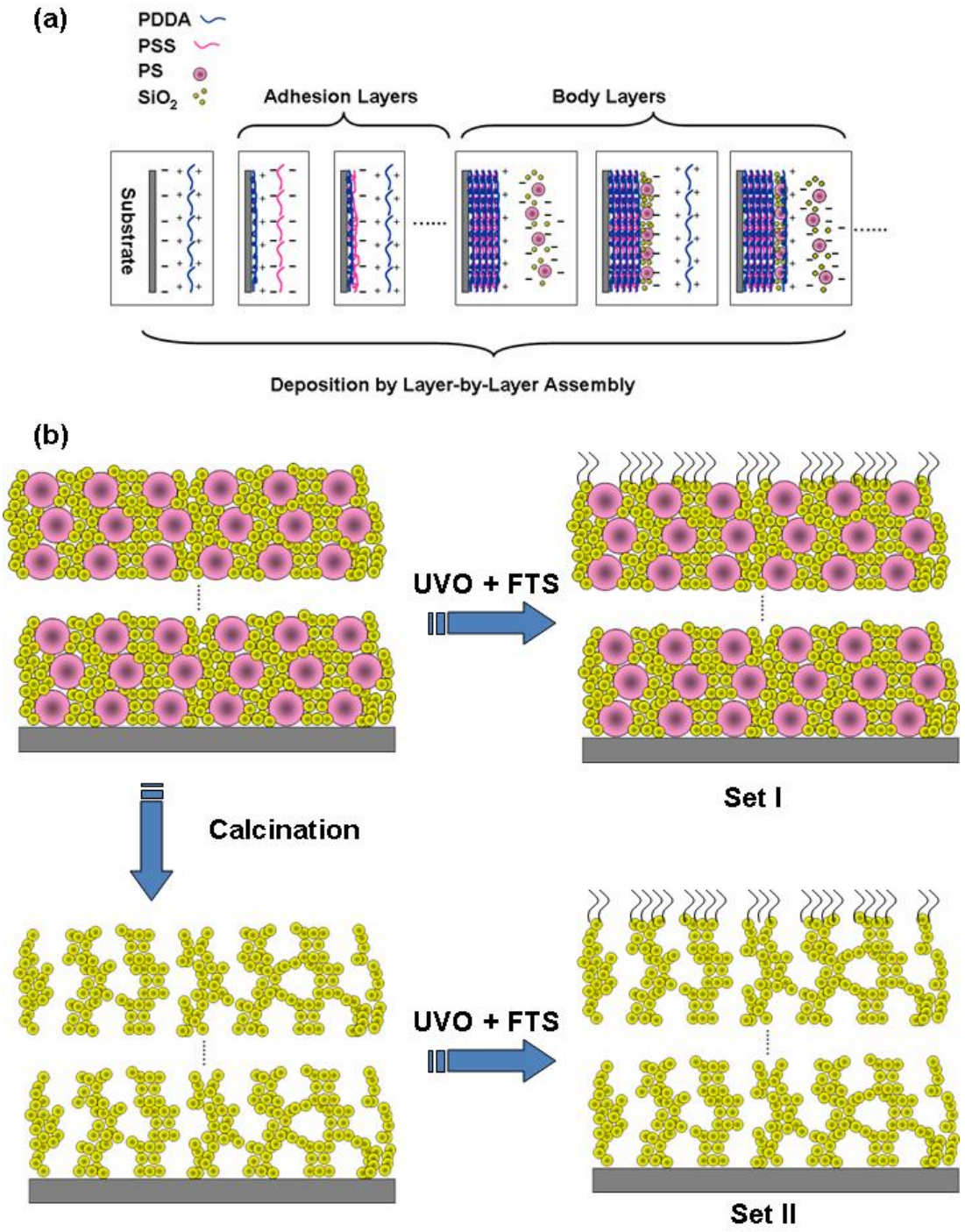

Figure 24. Schematic process for preparing the coatings. (a) Layer-by-layer assembly of 20 nm silica (SiO_2) nanoparticles and 60 sacrificial polystyrene (PS) nanoparticles. Adhesion layers are deposited before the deposition of body layers. (b) The assembled nanocomposite coating is treated by UVO and functionalized by FTS either directly after the assembly or after removal of the sacrificial PS particles through calcination.

nanoparticles by calcination. The layer-by-layer assembly process employed here is similar to previously published methods [47, 48], which are based on deposition of positively and negatively charged particles, polymers, or particle-polymer complexes alternately in sequential cycles. In our process, five bilayers of PDDA and PSS, $[PDDA/PSS]_5$, were first deposited as adhesion layers. Then, samples with 5, 10, 15, 20 and 25, bilayers of nanoparticles, $[PDDA/ (60 \text{ nm polystyrene} + 20 \text{ nm } SiO2)]_x$ (where x denotes the number of body bilayers), respectively, deposited on top of the adhesion layers were prepared. By virtue of electrostatic interactions involved in this process, organic–inorganic nanocomposite coatings consisting of different numbers of body layers were readily achieved. As expected, the thickness and the roughness of the coatings monotonically increased in a well controlled manner with increasing numbers of bilayers. This feature of the layer-by-layer assembly technique provides us with the capability to gradually tune the surface roughness and study its effect on the wettability and transparency of the coatings, and is particularly advantageous when both superhydrophobicity and transparency are desired.

For each coating of $[PDDA/(60 \text{ nm polystyrene} + 20 \text{ nm } SiO_2)]_x$, two sets of samples were prepared and compared. One set was treated by UV ozone and functionalized by FTS without removing the sacrificial polystyrene particles, while the other set was calcined to remove the sacrificial polystyrene particles before it was functionalized with FTS. Figure 25 shows the SEM images of the coatings with 25 bilayers before and after removing the polystyrene particles. As shown in Figure 25a, after the layer-by-layer assembly process, the smaller-sized silica particles (ca. 20 nm) crowd around the bigger-sized polystyrene particles (ca. 60 nm). After the calcination process, the bigger sacrificial polystyrene particles are removed (Figure 25b) while

leaving behind cavities with a similar size and shape, resulting in a porous network of silica nanoparticles.

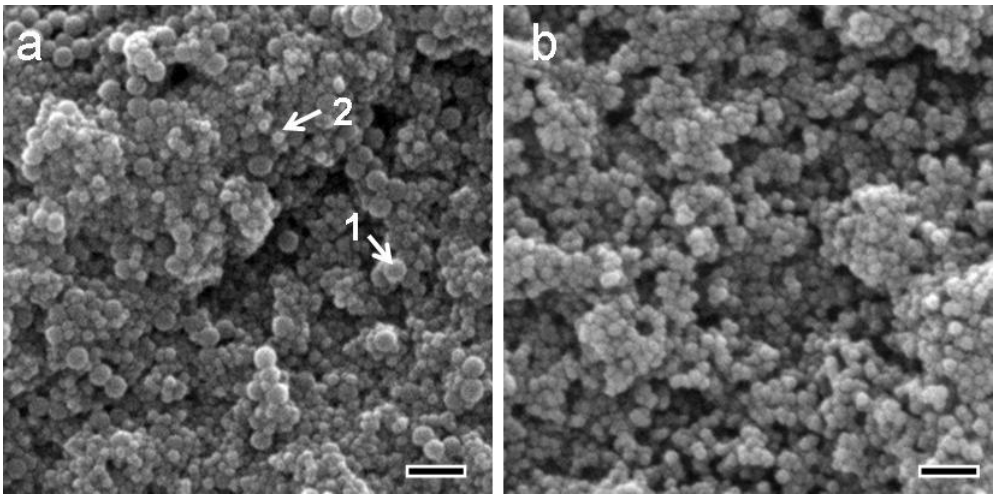

Figure 25. SEM images of the coatings. (a) and (b) are SEM images of the coatings with 25 bilayers before and after removing the sacrificial polystyrene particles, respectively. Labeled in (a) are a representative 60 nm polystyrene particle (labeled by "1") and a representative 20 nm silica particle (labeled by "2"). The polystyrene particles disappear in (b) after calcination. The scale bars are 200 nm.

After functionalizing both sets of samples with FTS, the hydrophobicity of these coatings is examined. Figs. 26a and b present the advancing and receding angles of water droplets on these two sets of coatings as a function of the number of the bilayers. On the first set of coatings which are prepared without removing the sacrificial polystyrene particles, the advancing angles are all in excess of 150°. However, large contact angle hysteresis (the difference between the advancing and the receding angles) of more than 90° is observed on all these samples and it increases with increasing the number of the bilayers. The combination of large advancing angles

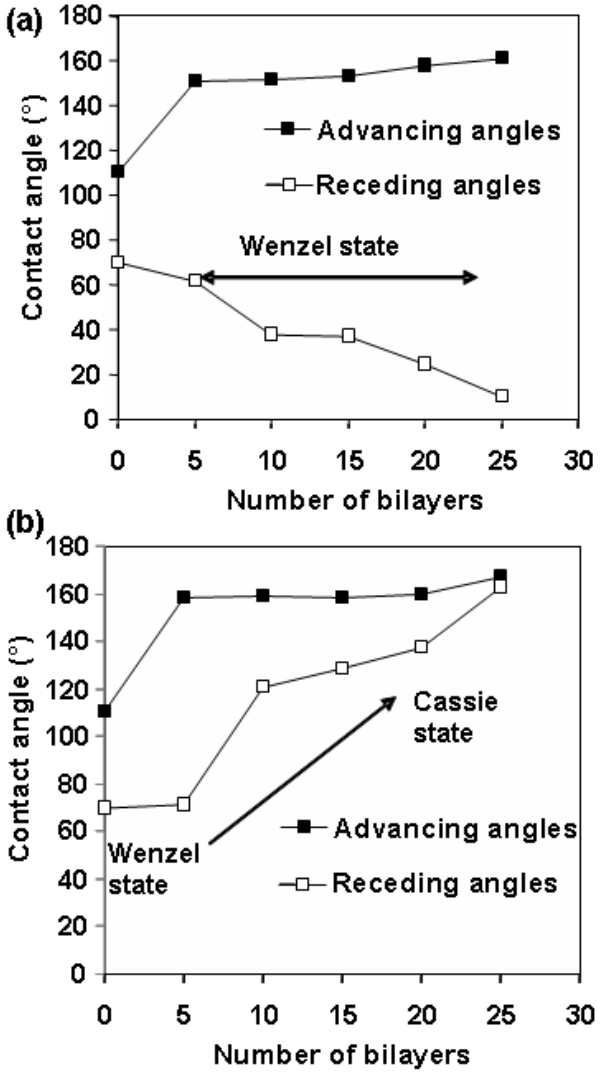

Figure 26. Advancing and receding contact angles as a function of the number of the bilayers on (a) the first set of coatings that are prepared without removing the sacrificial polystyrene particles and (b) the second set of coatings that are prepared after removing the sacrificial polystyrene particles.

and large hysteresis indicates that water droplets on these surfaces are most likely in a Wenzel state. In the Wenzel state, water is in complete contact with the rough solid surface, and the

apparent contact angle on the rough surface (θ_{rough}) can be correlated to the intrinsic contact angle of the solid surface (θ_{flat}) by the Wenzel's equation (Eqn. 3). Since θ_{flat} of the FTS-grafted surface is ~ 110°, according to Eqn. 3, θ_{rough} will increase as *r* increases. Therefore, as the number of the bilayers increases and thus *r* increases, the advancing contact angle of the coatings increases. On the other hand, water droplets in the Wenzel state on a rough surface are known to exhibit a large hysteresis, which is also consistent with our result.

During the wettability test on the second set of the coatings which are essentially porous networks of silica nanoparticles after removing the polystyrene particles, a transition in the wetting regime is clearly observed as the number of bilayers increases. As seen in Figure 26b, the advancing contact angles on this set of samples are all greater than 150°, but the hysteresis decreases significantly from ~ 87° for 5 bilayers to ~ 4° for 25 bilayers. When the number of bilayers is small, both the advancing contact angle and the hysteresis are large, which is similar to what has been observed on the first set of samples. Therefore, the system is in the Wenzel wetting regime. However, as the number of bilayers increases to 25, both a large advancing contact angle and small hysteresis are observed, which indicates that the system is in the Cassie wetting regime. When the number of bilayers is between 5 and 25, water droplets on the coatings gradually transit from the Wenzel state to the Cassie state.

In the Cassie state, liquid is in contact with a composite surface of solid and air, and forms droplets (known as fakir droplets). The apparent contact angle θ_{rough}, in this case, has been correlated to θ_{flat} by the Cassie–Baxter equation. By setting the Wenzel and Cassie-Baxter equations equal to each other, one can solve θ_{flat}, which corresponds to a critical angle θ_c which is greater than 90°, as determined by Eqn. 5. When $\theta_c < \theta_{flat}$, the Cassie state is

thermodynamically more favorable; otherwise, the Wenzel state is preferred. We believe that a decrease in θ_c is responsible for the transition of the system from the Wenzel state to the Cassie state as the number of bilayers increases. Because the roughness of the coating and thus *r* increases with increasing the number of bilayers, θ_c decreases according to Eqn. 5. θ_{flat}, on the other hand, is determined by the surface chemical composition of the coating, which in this case is the tethered FTS molecule. This means that θ_{flat} does not change significantly with the number of bilayers. Therefore, it is very likely that as the number of bilayers increase, θ_c will change from a value that is originally greater than θ_{flat} to a value that is smaller than θ_{flat}. Correspondingly, the system transits from the Wenzel to the Cassie wetting regimes.

The difference between the completely two different states that water is in on the two sets of coatings, before and after the sacrificial polystyrene particles are removed, respectively, may also be explained by the decrease in θ_c. As presented in Figure 26b, removal of polystyrene particles will create cavities between the network of silica particles and apparently will increase the actual solid surface area and hence *r*. This, in turn, will result in a decrease in θ_c. Because the difference in θ_{flat} between the two sets of these coatings is very small, θ_c could decrease from a value that is greater than θ_{flat} when the polystyrene particles are not removed, to a value that is smaller than θ_{flat} after the polystyrene particles are removed. We believe that this decrease of θ_c accompanying the removal of the polystyrene particles induces the Wenzel-to-Cassie wetting regime transition.

In addition to the much larger *r* which induces the wetting regime transition of water on the coatings, removal of sacrificial polystyrene particles creates an important surface texture on the coating surfaces, known as “overhang” [51-53] or “re-entrant” [40] structures. Such surface

textures are able to induce a metastable Cassie state when liquid is in contact with the rough solid surface even when θ_{flat} is less than 90° and certainly less than θ_c. The application of this mechanism to our system results in a coating that repels both water and oil with low surface tensions such as hexadecane (surface tension ca. 27.5 mN/m). Figs. 27a and b present photographs of a glass slide coated with 25 bilayers of polystyrene and silica nanoparticles, followed by calcination and functionalization with FTS. Both water and hexadecane form small beads when they are in contact with the coating. The contact angle of water is in excess of 160° with a small hysteresis of less than 5°. The contact angle of hexadecane on the coating is in excess of 140°, although the θ_{flat} of the FTS-grafted surface for hexadecane is only about 70°, which is much less than 90°. We believe that this high oil repellency of the coating is induced by the overhang structures on the surface which is formed during the removal of the sacrificial polystyrene particles.

Remarkably, the superhydrophobic and highly oil-repellent coating fabricated by this approach is also highly transparent. Because the polystyrene particles employed in this process are opaque, the transparency of the nanocomposite coatings fabricated by the layer-by-layer assembly process gradually decreases with increasing the number of the deposited bilayers during the assembly process. This effect becomes more apparent as the number of the bilayers exceeds 15, when the glass slide starts turning translucent. However, after the polystyrene particles are removed in the calcination step, the transparency of the glass slide recovers. This is evident from the photographs shown in Figs. 27a and b where the glass slide has been coated with 25 bilayers. Comparison of the transmission spectra of the glass slide before and after the coating process (shown in Fig. 27c) indicates that no significant decrease in the transparency of

the glass slide is observed after it is coated, which further proves the high transparency of the coating.

3.4.3 Conclusions

We have demonstrated that a transparent superhydrophobic and highly oleophobic coating can be fabricated based on a porous network of nanoparticles. The porous network can be constructed by first assembling an organic–inorganic nanocomposite and then removing the organic moieties by calcination. One example of this approach that we have shown in this work is to first construct a silica-polystyrene nanocomposite by using a layer-by-layer assembly technique and then remove the sacrificial polystyrene particles by calcination. The resulting nanoporous structure is highly transparent and can be made both superhydrophobic and highly oleophobic after functionalization with a fluorocarbon molecule. We believe that removal of the polystyrene particles from the nanocomposite forms overhang structures on the surface of the nanoporous structure, which induces the high oil-repellency of the coating even though the intrinsic oil contact angle of the solid surface is less than 90°. Although transparent superhydrophobic coatings have been demonstrated using the layer-by-layer assembly technique previously, to the best of our knowledge, this is the first time the fabrication of transparent coatings that are both superhydrophobic and highly oleophobic by using the layer-by-layer assembly technique has been demonstrated. In addition, a key innovation in our process is the employment of sacrificial organic particles, which not only form overhang structures for inducing the oil-repellency but also saves the final step of adding a top layer of smaller particles which has been previously employed in the literature for making transparent superhydrophobic coatings.

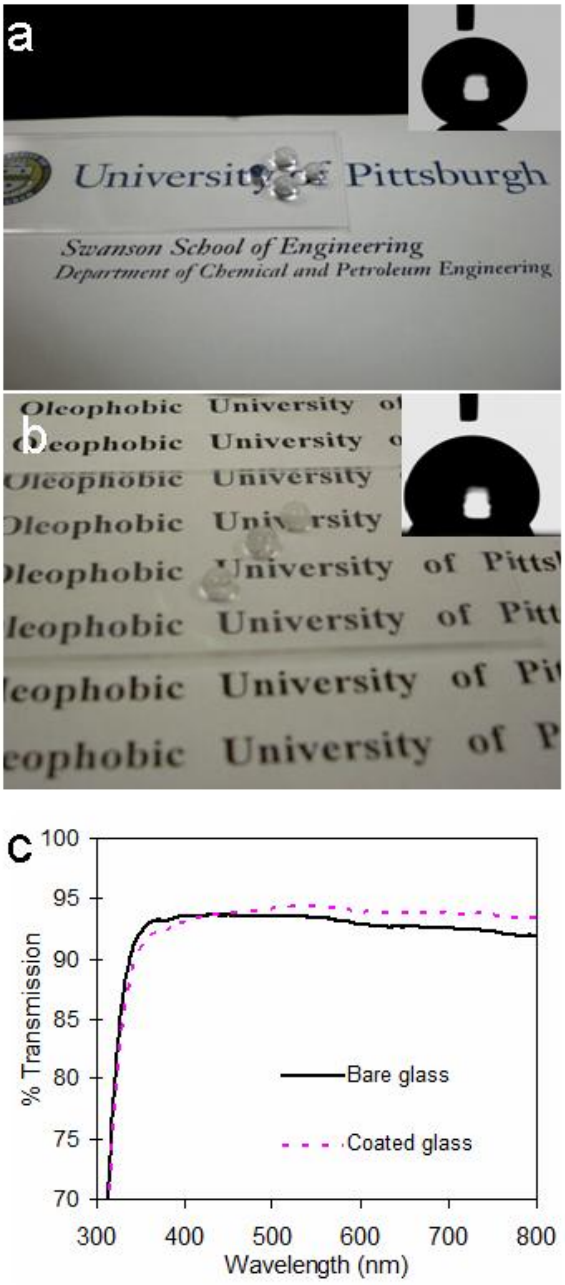

Figure 27. Photographs of a coated glass slide with droplets of (a) water and (b) hexadecane to demonstrate the superhydrophobicity, high oil-repellency, and transparency of the coating. Insets in (a) and (b) are images taken during the contact angle measurement. (c) Transmission spectrum of the glass slide before and after the coating process. The glass slide is coated with 25 bilayers, and is calcinated and functionalized with FTS.

4.0 APPLICATIONS OF SUPERHYDROPHOBIC SURFACES

4.1 ANTI-ICING

4.1.1 Introduction

One attractive application of superhydrophobic surfaces, in addition to the extraordinary water-repellency, is their speculated capability to reduce accumulation of snow and ice and to even completely prevent formation of ice on solid surfaces. Several groups have studied the adhesion of ice on superhydrophobic surfaces and have found correlations, with a reasonable degree of success, between reduction in ice adhesion and the superhydrophobicity of surfaces [54-56]. However, we are unaware of published research to study ice formation on superhydrophobic surfaces.

Among numerous problems caused by icing, many are due to striking of supercooled water droplets onto a solid surface. Such icing caused by supercooled water, also known as "freezing rain", "atmospheric icing", or "impact ice", is notorious for glazing roadways, breaking tree limbs and power lines, and stalling airfoil of aircrafts, which may cause immeasurable economic losses [57, 58]. Whereas extensive work has been published on superhydrophobicity, up to date there is little experimental/theoretical work on ice formation from supercooled water on superhydrophobic surfaces. The speculation on the anti-icing property of superhydrophobic

surfaces, especially when supercooled water droplets strike such surfaces, has been under debate for many years. However, up to date, no literature has clearly discussed ice formation of supercooled water on superhydrophobic surfaces. As a result, the speculation on the anti-icing property of superhydrophobic surfaces, especially when supercooled water droplets strike such surfaces, has been under debate for many years.

In this work, we study the anti-icing property of superhydrophobic coatings prepared by using nanoparticle-polymer composites. We demonstrate that when the size of the particles in these composites is in the right range, the coatings are able to prevent ice formation upon impact of supercooled water both in laboratory conditions and in naturally occurring environments. More importantly, we find that the anti-icing capability of these composites depends not only on their superhydrophobicity but also on the size of the particles exposed on the surface. The critical particle sizes that determine the superhydrophobicity and the anti-icing property are in two different length scales. These results open up possibilities for rational design of anti-icing superhydrophobic surfaces by tuning surface textures in multiple length scales.

4.1.2 Experimental section

Synthesis of acrylic polymer resin. In a typical process, the acrylic polymer was synthesized by a free radical polymerization of styrene, butyl acrylate, butyl methacrylate, and glycidyl methacrylate in toluene using azodiisobutyronitrile (AIBN) as the initiator. All these chemicals were purchased from Sigma-Aldrich. In a three-necked round-bottomed flask equipped with a magnetic stirrer, a condenser, a funnel, and a thermometer, 3.13 g styrene, 1.92 g butyl acrylate, 12.32 g butyl methacrylate, 4.25 g glycidyl methacrylate, and 100 ml toluene were mixed. The mixture was stirred and heated to 85 ^{o}C. Then, the heat source was turned off. A solution of 0.2

g AIBN in 2.5 ml toluene was dropwise added into the flask. The reaction mixture was heated to 85 ^{o}C and stirred isothermally for 3 hr. Afterwards, the same amount of AIBN toluene solution was added into the flask, and the mixture was stirred for another 3 hr. At the end of the reaction, the mixture was cooled at room temperature. The resulting acrylic polymer was precipitated in hexane and filtered, and then dried under vacuum at 40^{o}C for 24 hr.

Preparation of the polymer binder. In a typical process, the polymer binder was prepared by mixing 2.2 g of the synthesized acrylic polymer, 1.2 g of silicone resin (DOW CORNING® 840 RESIN, 60 wt% in toluene), 1.3 g toluene, and 0.6 g acetone. The binder can be cured either at room temperature for 12 hr or at 80 ^{o}C for 2 hr. During the curing process, the reactive glycidyl groups on the acrylic polymers crosslink with the silicone resin. The static water contact angle of the cured binder is ~107^{o}.

Preparation of the particle-polymer composites. The particle-polymer composites were prepared by mixing about 2.5 g of the organosilane-modified silica particles in varied diameters (20 nm, 50 nm, 100 nm, 1 μm, 10 μm, and 20 μm) with 5 g of the polymer binder, 75 g toluene, and 15 g acetone. They were applied on Al plates by a spray gun at a pressure of about 30 psi and cured at room temperature for 12 hr.

Electron microscopy. SEM images were taken on a Philips XL-30 field emission SEM setup. A thin palladium/gold film was sputtered on the sample before SEM images were taken. Transmission electron microscopy images were taken using a JOEL 200CX microscope.

Contact angle measurement. The water contact angles were measured by using a VCA-OPTIMA drop shape analysis system (AST Products, Inc.) with a computer-controlled liquid dispensing system and a motorized tilting stage. Water droplets with a volume of 4 μl were used to measure the static water contact angle. The advancing and receding angles were recorded during expansion and contraction of the droplets induced by placing a needle in the water droplets and continuously supplying and withdrawing water through the needle. The sliding angle was measured by tilting the stage and recorded when the droplet began to move in the downhill direction. Each measurement was repeated 3 times. The measurement was performed under normal laboratory ambient conditions (20 ℃ and 30% relative humidity).

Icing experiments using laboratory-made supercooled water. Supercooled water was prepared by storing bottled pure water in a -20 ^{o}C freezer for 3 hr. The coated and uncoated Al plates were also stored in the -20 ^{o}C freezer for 3 hr before the experiments and were tilted at an angle of about 10 ^{o} to the horizontal plane during the experiments. Supercooled water was poured onto the Al plates about 5 cm above the plates. Each experiment was repeated 20 times to obtain the probability of ice formation on different samples.

Icing experiments using naturally occurred freezing rain. One side of an Al plate (10 cm×10 cm) was coated with a superhydrophobic composite made with ~ 50 nm organosilane-modified silica particles, while the other side was untreated. A hole of about 1 cm in diameter was drilled near one edge of the plate and a cotton thread was used to hang the Al plate outdoors. Half of a commercial satellite dish antenna (SuperDish Network) was coated with the same composite while the other half was untreated. Both the dish antenna and the Al plate were placed outdoors

in a typical whether condition (~ -10 ^{o}C) of Pittsburgh, PA, in January for 7 days before the freezing rain occurred on the night of January 27, 2009.

4.1.3 Results and discussion

We made a series of particle-polymer composites by mixing a polymer binder with silica particles ranging from 20 nm to 20 μm in diameter. The polymer binder was synthesized by cross-linking a silicone resin with an acrylic polymer. The polymer binds strongly to many substrates including metal and glass, and has an intrinsic water contact angle of ~107°. The surface of silica particles was modified with organosilane molecules. The intrinsic water contact angle of the surface-modified silica particles is ~110°. The mixtures were sprayed onto aluminum (Al) plates and cured at room temperature for 12 hr.

The measured water contact angles of these composites are plotted in Figure 28. All the cured composites exhibit high water repellency. The composites prepared by using particles of 20 nm, 50 nm, 100 nm, 1 μm, and 10 μm in diameter all possess similar superhydrophobicity, characterized by the larger than 150° advancing and receding angles with less than 2° hysteresis. Only the composite prepared by using 20 μm particles has a less than 150° water contact angle and about 4° hysteresis. To test the anti-icing capability of these composites, we poured supercooled water (T = −20 ^{o}C) onto the coated Al plates from ~5 cm above and visually inspected whether ice was formed upon the impact. Figure 29 shows typical images taken during the experiment, which demonstrates the anti-icing property of the superhydrophobic nanoparticle-polymer composites. During the experiment, supercooled water (-20 ℃) was poured onto two Al plates. The right plate was untreated, while the left one was coated with a nanoparticle-polymer composite (with 50 nm particles). On the right plate, ice formed instantly

when the supercooled water impacted the plate. In contrast, on the left, ice did not form when the supercooled water impacted the plate, but built up from the bottom edge where the plate was in contact with an untreated Al tray. It is evident that the coating on the left Al plate is very effective to prevent icing of supercooled water upon striking the surface.

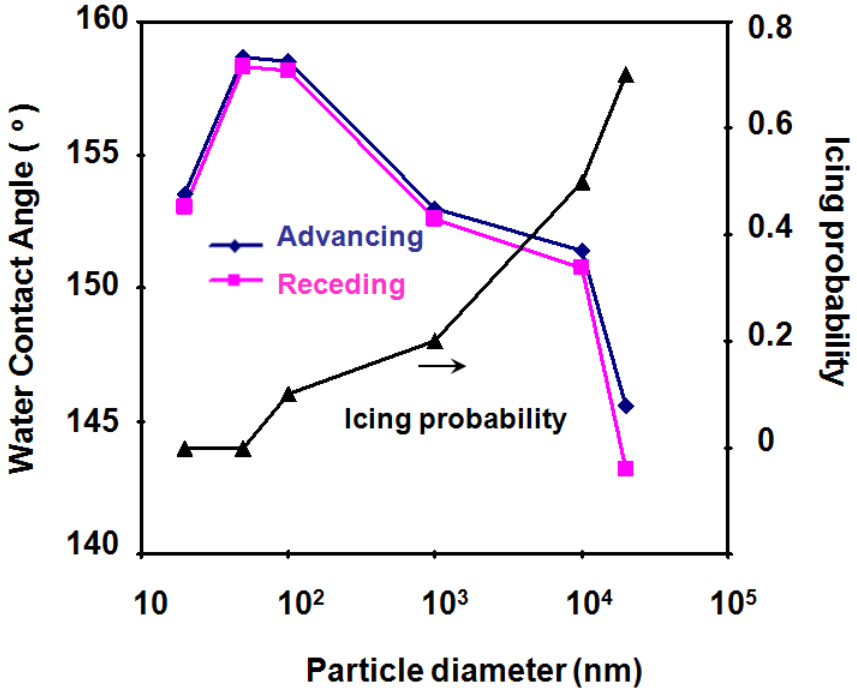

Figure 28. Probability of ice formation and the advancing and receding angles of water droplets on each particle-polymer composite as a function of the particle size.

The experiment was repeated 20 times for each sample to obtain the probability of ice formation. The result is shown in Figure 28, where the icing probability is plotted with the contact angles as a function of the size of the particles used in the composites. It is observed that the critical particle sizes that determine the superhydrophobicity and the anti-icing property,

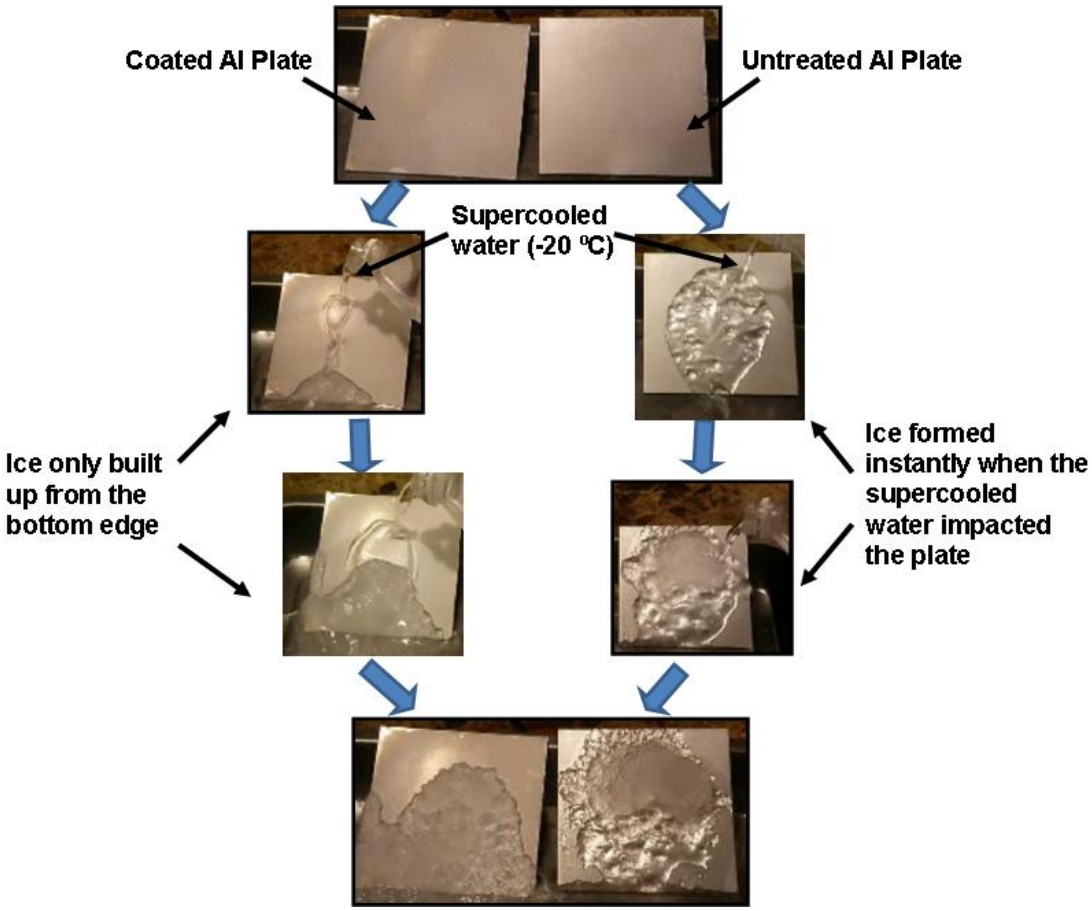

Figure 29. Optical images taken during the icing experiment, demonstrating the anti-icing property of a superhydrophobic nanoparticle-polymer composite. Supercooled water (-20 ℃) was poured onto two Al plates. The right plate was untreated, while the left one was coated with a nanoparticle-polymer composite (with 50 nm particles). On the right plate, ice formed instantly when the supercooled water impacted the plate. In contrast, on the left, ice did not form when the supercooled water impacted the plate, but built up from the bottom edge where the plate was in contact with an untreated Al tray.

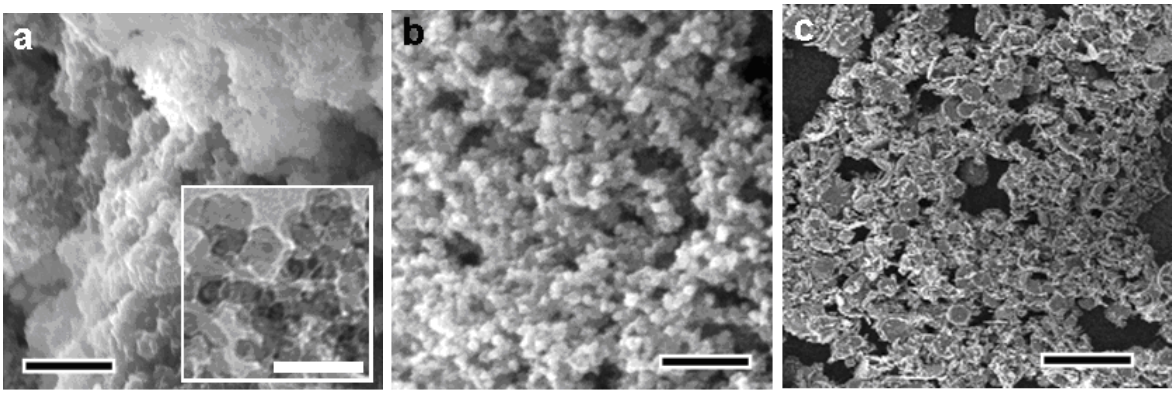

Figure 30. Representative electron microscopy images of particle-polymer composites. a, Scanning electron microscopy (SEM) image of a particle-polymer composite made with 20 nm silica particle. Scale bar, 1 μm. Inset, transmission electron microscopy image. Scale bar, 50 nm. b, SEM image of a particle-polymer composite made with 50 nm silica particles. Scale bar, 1 μm. c, SEM image of a particle-polymer composite made with 20 μm silica particles. Scale bar, 100 μm.

respectively, are in two different length scales. Although composites made with particles up to 10 μm in diameter are all superhydrophobic, the anti-icing capabilities of these coatings are distinctly different—ice does not form on the samples prepared with 20 and 50 nm particles at all, but the icing probability increases remarkably when the particle diameter is larger than 50 nm. Figure 30 shows three representative electron microscopy images of the cured composites with 20 nm, 50 nm and 20 μm particles, respectively. Based on these images, the structure of the composites and the profile of water in contact with the composites are schematically shown in Figure 31a. Water on these composites is primarily in contact with air pockets trapped in the rough surfaces. According to the Cassie-Baxter equation, the large water contact angles on these composites imply that only less than 15% of the solid part is in direct contact with water. Therefore, when supercooled water impacts such surfaces, icing may occur through a heterogeneous nucleation process at the contact between water and the particles exposed on the

surfaces. As a result, the kinetics of the ice nucleation process is determined by the size of the particles exposed on the surfaces.

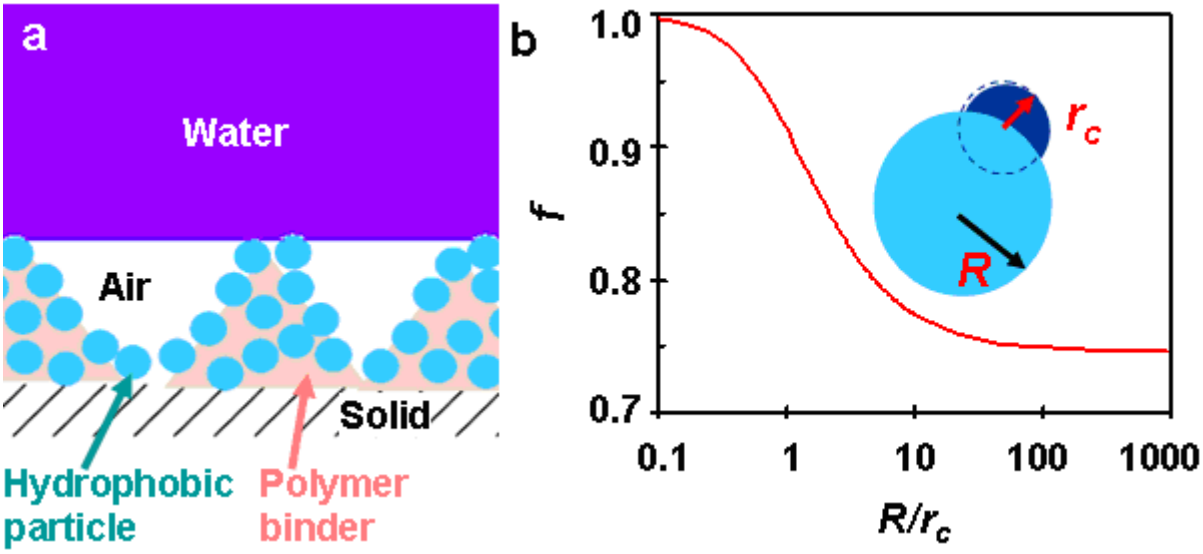

Figure 31. Heterogeneous nucleation on the surface of a superhydrophobic particle-polymer composite. (a) Schematic cross-sectional profile of water in contact with a superhydrophobic particle-nanoparticle composite. (b) Ratio (*f*) of the free-energy barrier for nucleation around a spherical particle relative to that in the bulk versus the relative particle radius (R / r_c).

The effect of the particle size on the energy barrier encountered by the heterogeneous nucleation process can be estimated by using a classical heterogeneous nucleation theory [59]. The free energy barrier for heterogeneous nucleation (ΔG_c) around a spherical particle of radius (R) is reduced by a factor (f) in comparison with that for homogeneous nucleation (ΔG_c^{homo}):

$$\Delta G_c = \Delta G_c^{\text{homo}} \times f , \qquad (7)$$

where f varies from 1 to 0. The effect of particle size on f can be calculated by:

$$f = \frac{1}{2} + \frac{1}{2}\left(\frac{1-mx}{w}\right)^3 + \frac{x^3}{2}\left[2 - 3\left(\frac{x-m}{w}\right) + \left(\frac{x-m}{w}\right)^3\right] + \frac{3mx^2}{2}\left(\frac{x-m}{w} - 1\right), \quad (8)$$

where r_c is the radius of the critical nucleus, $x = R/r_c$, $m = \cos\theta_{flat}$ with $\theta_{flat} = 110^\circ$ for the hydrophobic silica particles, and $w = (1 + x^2 - 2xm)^{1/2}$. According to classical nucleation theory, the radius of the critical nucleus (r_c) can be estimated by:

$$r_c = -\frac{2\gamma v}{\Delta G}, \quad (9)$$

where $\gamma \approx 0.034$ J m^{-2} is the water-ice interfacial tension [60], $v \approx 1.8\times10^{-5}$ m^3 mol^{-1} is the water molar volume, and $\Delta G \approx -C_p T\left[\ln(T/T_m) + T_m/T - 1\right]$. In this work, T = 253.15 K (-20 ^{o}C), the ice melting temperature is T_m = 273.15 K (0 ^{o}C), and water heat capacity is $C_P \approx$ 75.3 J mol^{-1} K^{-1}. r_c is calculated to be 21.6 nm under our experimental conditions.

Figure 31b presents the dependence of f on the relative particle radius (R/r_c) according to Eqn. 8. It shows that f falls monotonically as R increases, which implies that the energy barrier (ΔG_c) continuously decreases as the particle size increases. Because the icing probability is an exponential function of the free energy barrier, the observed dramatic increase of the icing probability as the particle size increases can be readily explained.

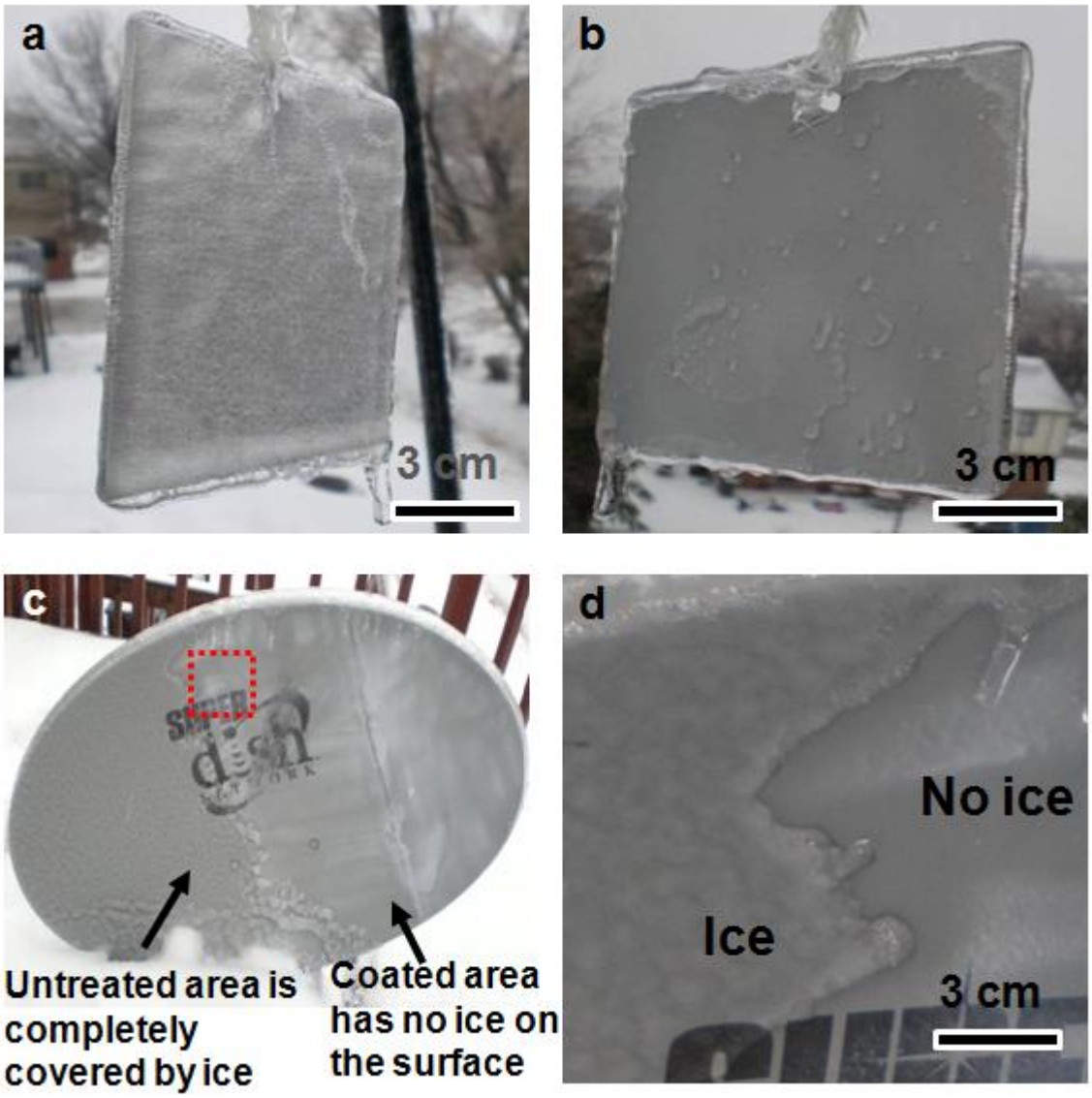

Figure 32. Test of anti-icing properties in naturally occurring "freezing rain". (a) Untreated side of an aluminum plate after the natural occurrence of "freezing rain". (b) Treated side of the aluminum plate coated with a superhydrophobic composite after the "freezing rain". (c) Satellite dish antenna after the freezing rain. The left side is untreated and is completely covered by ice, while the right side is coated with the superhydrophobic coating and has no ice. (d) Close-up view of the area labeled by a red square in (c), showing the boundary between the coated (no ice) and uncoated area (ice) on the satellite dish antenna.

We have also tested the anti-icing properties of the superhydrophobic composite in naturally occurred freezing rain. We coated one side of an Al plate with the composite made with 50 nm particles and left the other side untreated. The plate was left outdoors in winter for a week before freezing rain occurred. Figs. 32a and b show the two sides of the Al plate after the freezing rain: the side with the superhydrophobic composite has little ice, while the untreated side is completely covered by ice. Similar results were also obtained on a commercial satellite dish antenna (Figs. 32c and d), where one half side of the dish was coated with the superhydrophobic composite and had no ice, but the other half was untreated and was completely covered by ice after the freezing rain. These results suggest significant application potential of the superhydrophobic nanoparticle-polymer composite as practical anti-icing coatings.

4.1.4 Conclusion

We have studied icing of supercooled water on superhydrophobic surfaces prepared using nanoparticle-polymer composites. We find that the anti-icing capability of these superhydrophobic coatings is dependent strongly on the size of particles. This critical size, interestingly, is in a significantly different length scale compared to the critical size that determines the superhydrophobicity of these surfaces. This implies that caution needs to be taken when the anti-icing property is correlated to the superhydrophobicity, and it is uncertain whether a superhydrophobic surface is anti-icing without detailed knowledge of the surface morphology. It is worth noting that the polymer binder synthesized and used in this work is not the only binder that may be used to make anti-icing superhydrophobic nanoparticle-polymer composites. We believe that many other polymer binders with a variety of compositions may also function in the same mechanism. Regardless of the composition of the coatings, it is

important to recognize the two different length scales that determine the superhydrophobicity and the anti-icing property. Icing of supercooled water on superhydrophobic surfaces is a complex phenomenon, and it may also depend on ice adhesion, hydrodynamic conditions, and structure of the water film on the surface. Further research is needed to understand the effect of these factors on icing. However, it is hoped that the experimental and theoretical results presented in this work may provide some insights into this complex phenomenon and open up possibilities for rational design of anti-icing superhydrophobic surfaces by tuning surface textures in multiple length scales.

4.2 INTERFACIAL SLIP AND DRAG REDUCTION

4.2.1 Introduction

As one of the core assumptions in fluid mechanics, the no-slip boundary condition is commonly applied in analyzing fluid flow past a solid surface, which has been well supported by numerous experimental results at macroscopic scales [61]. However, researchers have also reported evidence of interfacial slip over certain hydrophobic surfaces, and the fluid slippage has been attributed to a partial wetting effect occurring at the surfaces [62-67]. Recently, superhydrophobic surfaces, characterized by a very high water contact angle (typically greater than 150°) and low hysteresis, have received considerable attention due to their potential application in drag reduction. Water on such surfaces is in contact with a composite surface of

solid and air (known as the Cassie state), and a layer of air pockets is formed between water and the solid surface. Numerous experiments have demonstrated that an apparent fluid slippage may occur over superhydrophobic surfaces, which leads to significant hydrodynamic drag reduction [68-75]. As a result, researchers have proposed to use superhydrophobic surfaces inside pipes, tubes, and ducts to save energy for fluid transportation [68, 70, 71], and inside microchannels for facilitating fluid transport in microfluidics [74, 75].

First proposed by Navior [76], interfacial slip has been generally quantified by a parameter, the slip length b, which is defined by $v_s = b\left(dv_x / dy\right)$ (Fig. 33b), where v_s and $\left(dv_x / dy\right)$ are the macroscopic fluid slippage velocity and the shear rate at the solid-liquid interface, respectively, and y is the axis normal to the surface. According to this definition, if $b = 0$, the conventional no-slip boundary condition is obtained (Fig. 33a); if $b = \infty$, a shear-free boundary condition is obtained; otherwise, a partial slip boundary condition is obtained (Fig. 33b). Following this definition, researchers have been using the magnitude of the slip length b as an "effective" parameter to evaluate the slippery nature of superhydrophobic surfaces [74, 77, 78], *i.e.*, the greater the slip length, the more slippery the superhydrophobic surface. As a result, b has been used to define the boundary condition and to calculate hydrodynamic drag for flows past a superhydrophobic surface. Apparently, such an approach is under an assumption that, with a constant fluid density and viscosity, b is mainly dependent on the intrinsic properties of the superhydrophobic surfaces (*e.g.*, the water contact angle [70, 71], the morphology of the surface [77], and the thickness of the trapped air layer [74, 75]). Recently, a few experimental results suggest that certain flow properties, such as Reynolds number *Re* [72], and the characteristic length of the flow field [68], may also affect b. However, comprehensive research and systematic analysis on the dependence of b on the flow properties is currently lacking, although

the outcome of such research may challenge the generally accepted concept of using b to characterize the slippery nature of superhydrophobic surfaces.

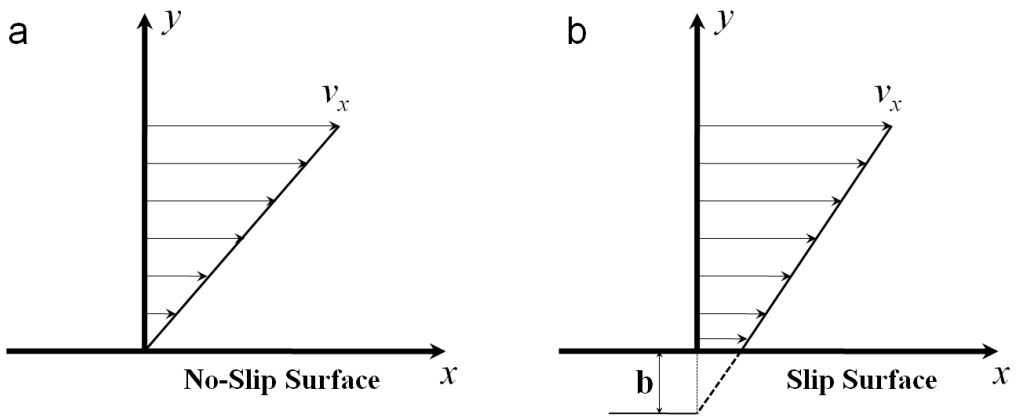

Figure 33. Schematic diagrams of boundary conditions. (a) No-slip condition. (b) Slip condition.

In this work, we investigate the dependence of b and friction drag reduction on Re for laminar flows between two superhydrophobic parallel plates through both numerical simulation and experimental approaches. Interestingly, it is found that in such a system, both b and the drag reduction, compared to the flow between two no-slip plates, are apparent functions of Re. When the friction drag and the pressure drop are characterized by using a phenomenological friction factor f, it is found that the relative reduction of f has an empirical linear relationship with Re.

4.2.2 Methodology

For a laminar flow between two infinite parallel plates separated by a distance H, the velocity profile can be described by (Appendix):

$$\mu \frac{d^2 v_x}{dy^2} - \frac{dp}{dx} = 0, \qquad (10)$$

where x is along the flow direction, μ is the viscosity of the fluid. With the no-slip boundary condition, *i.e.*, at $y = \pm H/2$, $v_x = 0$, the pressure gradient along the flow direction is:

$$-\left(\frac{dp}{dx}\right)_{no-slip} = \frac{6\mu^2 Re}{\rho H^3}, \qquad (11)$$

where ρ is the density of fluid, and $Re = \rho U D_h / \mu$ with U being the average velocity. This pressure gradient can also be described by using a phenomenological friction factor f by Darcy-Weisbach equation [79]:

$$f_{no-slip} = -2\left(\frac{dp}{dx}\right)_{no-slip} \frac{D_h}{\rho U}, \qquad (12)$$

where D_h is the hydraulic diameter (here $D_h \approx 2H$). For a laminar flow between two infinite parallel plates with no-slip boundary conditions, the friction factor $f_{no-slip} = 96/Re$ [79].

With a slip boundary condition, *i.e.*, at $y = H/2$, $v_x = -b\left(dv_x/dy\right)_{y=H/2}$ or at $y = -H/2$, $v_x = b\left(dv_x/dy\right)_{y=-H/2}$, solving Eqn. 10 gives the pressure gradient:

$$-\left(\frac{dp}{dx}\right)_{slip} = \frac{6\mu^2 Re}{\rho H^3\left(1+\frac{6b}{H}\right)}, \quad (13)$$

and thus the friction factor of the slip boundary conditions is:

$$f_{slip} = -2\left(\frac{dp}{dx}\right)_{slip}\frac{D_h}{\rho U} = \frac{96}{Re}\left(\frac{1}{1+\frac{6b}{H}}\right). \quad (14)$$

If R_f is defined as the relative reduction of the friction factor by $R_f = \frac{f_{no-slip} - f_{slip}}{f_{no-slip}}$, R_f can be correlated with b by $R_f = \frac{6b/H}{1+6b/H}$. Obviously, R_f is between 0 and 1, and is determined by $6b/H$. When the scale of $6b$ is comparable to H, a noticeable drag reduction may be observed, and the drag reduction becomes more significant with increasing $6b/H$. Recent measurements on the superhydrophobic surfaces have reported b in the range of several [70, 77] to tens of microns [74]. To obtain an appreciable R_f, H is selected to be ~ 100 μm for both numerical and experimental analysis in this work.

In the numerical approach, the dependence of b and R_f on Re is investigated by simulating laminar flows between two parallel plates using the finite element method (FEM). Pressure-driven laminar flows between two types of plates are simulated and compared: Type I plate is a solid plate with a smooth surface, where the no-slip boundary condition is applied; Type II plate is constructed by forming evenly spaced cavities on the surface to simulate a

superhydrophobic plate (Fig. 34). On the Type II plate, water is in contact with a composite surface of solid and air, known as the Cassie state. At the water-solid interface, the no-slip boundary condition is applied; at the water-air interface, the boundary condition is set to match both the momentum flux and the velocity between water and air. To make the plate superhydrophobic, the geometrical parameters of the textured surface (*i.e.*, the widths of the post l_s and the cavity l_a) on the Type II plate are designed according to the Cassie-Baxter equation $\cos\theta_{rough} = \phi_s \cos\theta_{flat} - (1-\phi_s)$. If θ_{flat} is assumed to be 110 º (in good agreement with most CH_3- and CF_3-terminated molecules), ϕ_s [here $\phi_s = l_s/(l_s + l_a)$] should be smaller than 0.20 in order to make θ_{rough} greater than 150 º. Therefore, we set l_s and l_a to be 10 μm and 40 μm, respectively, to make $\phi_s = 0.20$. The height δ of the post is set to be 20 μm. The two plates are separated by a distance H of 100 μm. For water, ρ and μ are set to be 1000 kg/m^3 and 0.001 Pa·s, respectively. The density and viscosity of air are set to be 1.2 kg/m^3 and 1.985×10^{-5} Pa·s, respectively. FEM simulations are conducted by using a commercial software, Comsol® for both types of the microchannels.

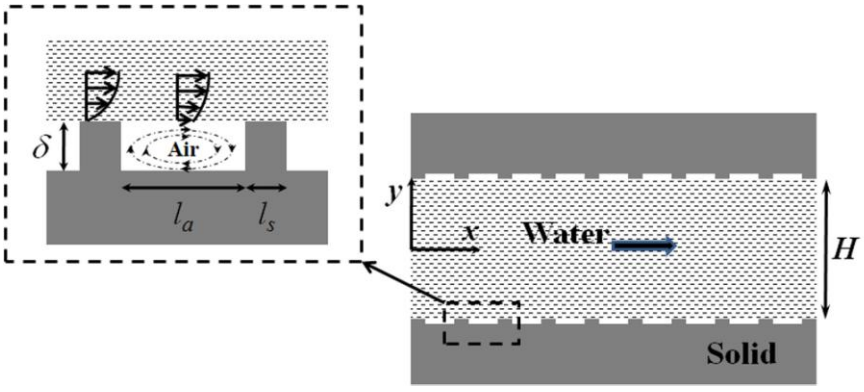

Figure 34. Schematic diagram of laminar flows between two infinite parallel plates with superhydrophobic surfaces. Water is in contact with a composite surface of solid and air. The flow direction is parallel to the *x*-axis.

In the experimental approach, the dependence of b and R_f on Re is investigated by posing laminar flows in a channel formed between two superhydrophobic plates and measuring the pressure drop along the flow. The channel is fabricated by machining a 100 μm deep groove on an aluminum (Al) plate, and covering the Al plate with a polydimethylsiloxane (PDMS) membrane, as schematically shown in Figs. 35a and b. The length L, height H and width W of the channel are 10 cm, 100 μm and 5 mm, respectively. Since W is far greater than H, the channel is a good approximation to the model of two infinite parallel plates. The PDMS membrane has 4 openings, and each opening is connected to a silicone tubing sealed by the epoxy resin. The 4 tubings are used to connect the channel to the pump and the pressure gauge. During the experiments, the PDMS membrane is tightly sealed with the Al plate by another covering Al plate with a rectangular opening. An infusion pump (Harvard Apparatus, Model PHD 2000) is used to drive the flow through the channel. A wet/wet differential pressure gauge (Omega PX26) is used to measure the pressure drop Δp along a fixed distance ΔL (5cm). The distance L_e (2cm) between the inlet opening and the upstream opening for the pressure measurement is much larger than the entrance length ($\sim 0.06 D_h Re$) of the flow. To make the Al plate and the PDMS membrane surface superhydrophobic, a nanoparticle-polymer composite [80] is applied on both substrates. Figure 35c shows the SEM image of the composite. The water contact angle on the coating is ~165^o (Fig. 35d). After measurement is completed using the superhydrophobic channel, the superhydrophobicity of the coating is removed by applying an O_2-plasma treatment (South Bay Technology model PC-2000 RF Plasma Cleaning System), and both the top and bottom plates become hydrophilic without apparent morphological change on the surface.

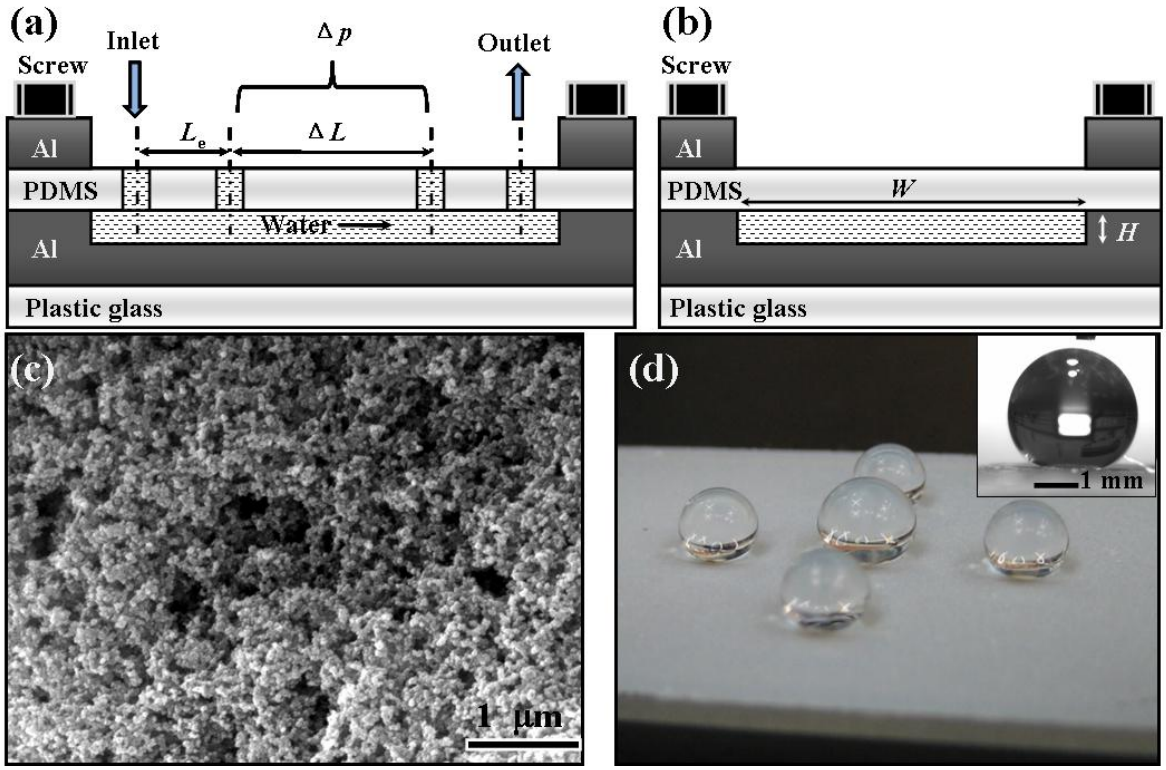

Figure 35. Experimental setup. (a) and (b) are schematic front and side views of the channel. (c) An SEM image of superhydrophobic nanoparticle-polymer composite coating. (d) Optical images of water droplets on the superhydrophobic coating.

4.2.3 Results and discussion

In the numerical approach, a series of flows between two types of plates with Re varying from 10 to 100 are simulated. Figs. 36a and b show typical snapshots of the velocity profiles generated by simulating flows (with $Re = 10$) between smooth solid plates and superhydrophobic plates, respectively. Two distinct velocity profiles are observed. It is of particular interest to

observe that on the superhydrophobic plate, the air trapped in the cavity undergoes a toroidal circulation (Rybczynski-Hadamard circulation), which is known to contribute to drag reduction [81].

The average pressure gradient in two types of channels obtained from the simulation is plotted in Figure 36c as a function of Re. For the Type I channel, the simulated pressure drop is in good agreement with the analytical solution obtained using the no-slip boundary condition (Eqn. 11). For the Type II channel, an apparently smaller pressure gradient can be observed compared to the no-slip case, which indicates significant drag reduction. From the pressure gradient in the superhydrophobic channel, slip length is calculated according to Eqn. 13 and is plotted in Figure 36d. The friction factors $f_{no-slip}$ and f_{slip} are calculated according to Eqns. 12 and 14, respectively, and the relative reduction of the friction factor R_f is plotted in the inset of Figure 36d. It is observed that there appears to be an empirical linear relationship between R_f and *Re*. We suggest that such a relationship be expressed as:

$$R_f = -\alpha Re + \beta, \quad (15)$$

where we may define α as attenuation coefficient and β as maximum relative drag reduction coefficient for a hydrodynamic system with defined superhydrophobic boundaries. That is, R_f is linearly attenuated with increasing Re by a rate α, and the maximum of R_f is β, which is approached when *Re* approaches zero. In this specific system, α is ~ 0.0006, and β is ~ 0.353.

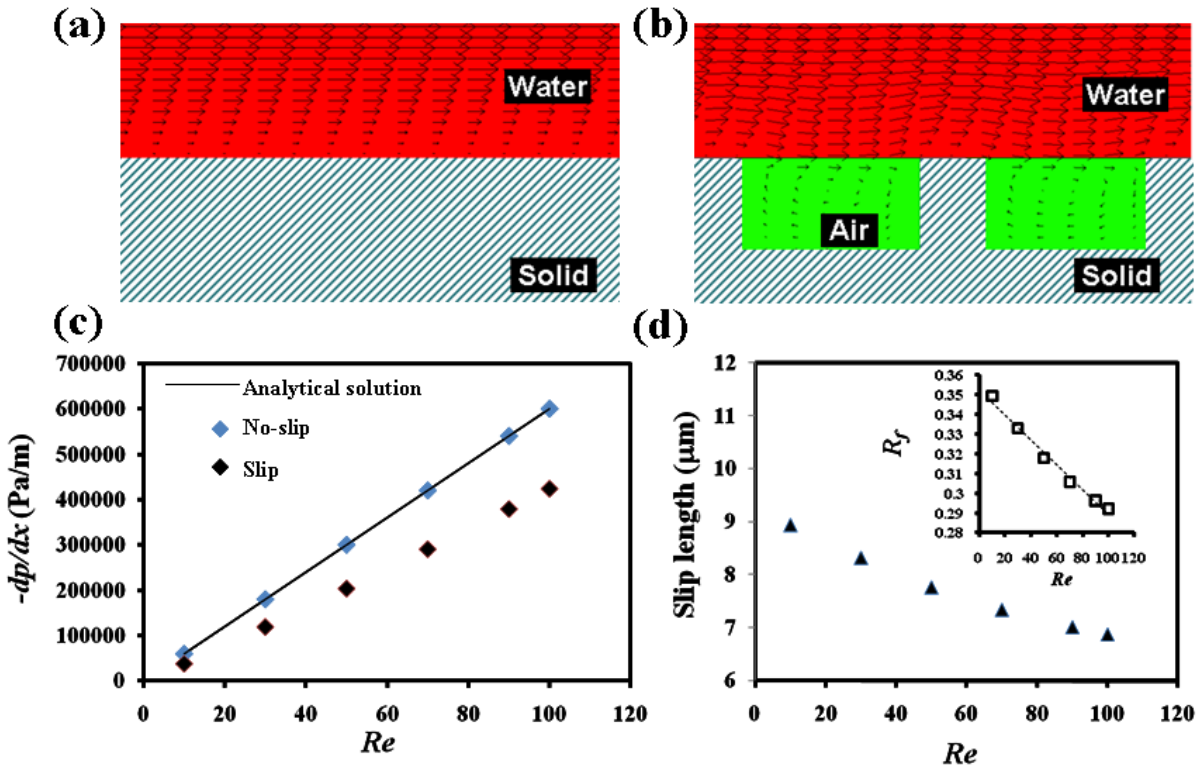

Figure 36. Simulation results. (a) and (b) are snapshots of the velocity profiles generated by simulating laminar flows (with Re = 10) in two types of channels formed between smooth solid plates and superhydrophobic plates, respectively. (c) Pressure gradient in two types of channels as a function of Re. The solid line is the analytical solution. (d) Slip length and the relative reduction of the friction factor R_f (inset) as a function of Re.

For the experimental results, Figure 37a shows the average pressure gradient measured as a function of Re. When the plates are hydrophilic (*i.e.*, with no-slip boundary conditions), the measured pressure gradient is in good agreement with the analytical solution. When the plates are superhydrophobic, the pressure gradient is apparently reduced, indicating interfacial slip on the superhydrophobic surface. From the pressure gradient, b and R_f are calculated and plotted in Figure 37b as a function of Re. Similar to the result obtained by numerical simulation, an approximate linear relationship is also obtained between R_f and Re through the experimental

approach. If R_f is written as a function of Re in the form of Eqn. 15, α is ~0.0012, which is greater than the α obtained by the numerical simulation, and β is ~ 0.212, which is smaller than the β obtained by the numerical simulation. This indicates that the influence of Re on the interfacial slip is stronger for the experimental system than for the simulation system, but the maximum R_f and b is smaller in the experimental system than in the simulation system. The reason for such a result may be attributed to the difference in various intrinsic surface properties (such as surface textures) between the plates used in experiments and in simulation. Although how α and β may be affected by the surface texture of a superhydrophobic surface is still unknown, our result clearly indicates that the slippery nature of a superhydrophobic surface would be more properly characterized by using α and β than by using b.

4.2.4 Conclusion

We have investigated interfacial slip on superhydrophobic surfaces and the resulting hydrodynamic drag reduction of laminar flows between two parallel plates through both numerical simulation and experimental approaches. Up to 20%-30% reduction in the friction factor has been observed by either approach. It has been observed that slip length, a parameter commonly used to characterize the slippery nature of superhydrophobic surfaces, significantly decreases with increasing Re. When the drag reduction is described by the relative reduction of the friction factor R_f, it is found that R_f has an empirical linear dependence on Re. We suggest that such a linear relationship be described by two phenomenological coefficients—attenuation coefficient and maximum relative drag reduction coefficient—for a hydrodynamic system with defined superhydrophobic boundaries. Such a linear relationship may provide a

convenient approach for calculating friction drag in hydrodynamic systems involving superhydrophobic surfaces.

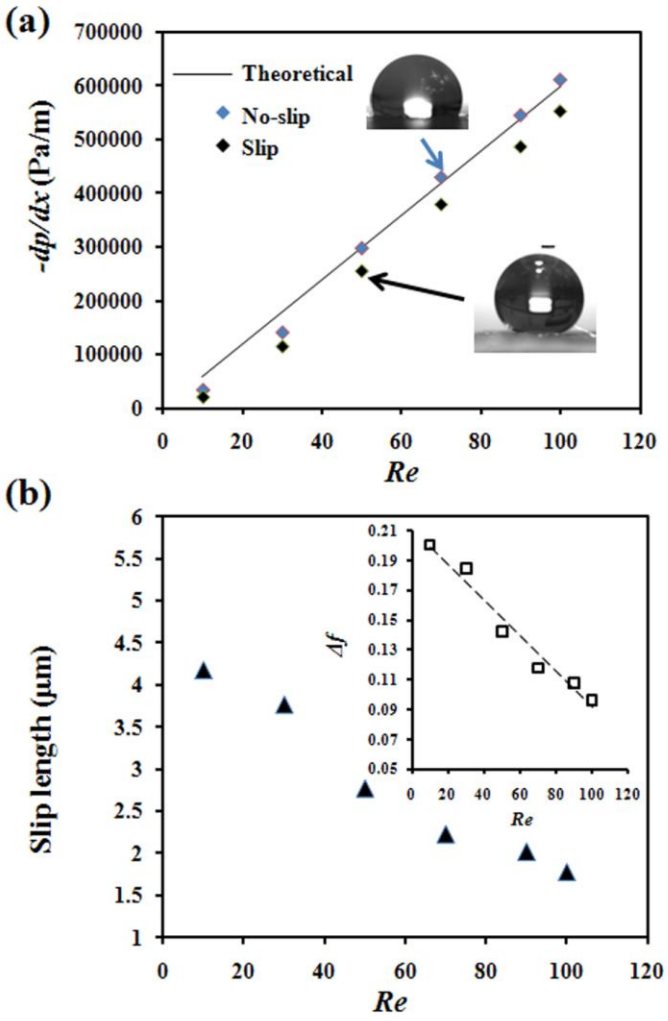

Figure 37. Data obtained from experimental results: (a) pressure drop measurements as a function of *Re*; (b) the influence of *Re* on the slip length as well as the drag reduction (inset).

5.0 SUMMARY

This dissertation consists of two major sections: the first section (1.0-3.0) focuses on the design and fabrication of superhydrophobic surfaces, and the second section focuses on the application (4.0) of such surfaces. In the first section, on the basis of a review of general principles and experimental methods for fabricating superhydrophobic surfaces, we introduce a novel design concept and develop practical schemes, which typically involve nanomaterial synthesis as well as micro- and nano-fabrication technologies, for making superhydrophobic surfaces on intrinsically hydrophilic materials. This design concept and the experimental methods for implementing it have also been employed to make superoleophobic surfaces that repel oil in the same way as superhydrophobic surfaces repel water. In the second section, we present our initial effort to explore two promising applications of superhydrophobic surfaces: one is to prevent supercooled water from icing; the other is to reduce friction drag of internal water flows. The primary accomplishments of the research outlined in this paper can be summarized as the following:

1. We have developed a general design principle for fabricating surfaces with special surface topographical textures (*e.g.*, overhang or re-entrant curvature) that may induce the superhydrophobic and/or superoleophobic phenomena on intrinsically hydrophilic and/or oleophilic substrates.

2. We have experimentally proved our design principle by fabricating Si micro-textures with well-defined overhang structures in both micrometer and nanometer scales, which are able to induce a superhydrophobic behavior on hydrophilic H-terminated silicon surfaces with a θ_{flat} of ~ 74°.
3. We have demonstrated that our design principle can be applied to fabricate non-aging superhydrophobic surfaces by packing flower-like hematite particles. These superhydrophobic surfaces do not age even in extremely oxidative environments—they are able to retain the superhydrophobicity after being stored in ambient laboratory air for 4 months, heated to 800 ℃ in air for 10 hours, and exposed to ultraviolet ozone for 10 hours.
4. We have demonstrated that our design principle can be extended to fabricate super oil-repellent surfaces on intrinsically oleophilic substrates using porous Si films as an example. The porous Si films are fabricated by a gold-assisted electroless etching process, which produces a hierarchical porous structure that consists of micrometer-sized asperities superimposed onto a network of nanometer-sized pores. Contact angles of greater than 150 ° for both diethylene glycol and hexadecane have been obtained on porous Si surfaces after surface treatment.
5. We have demonstrated that a transparent superhydrophobic and highly oleophobic coating can be fabricated based on a porous network of nanoparticles by using a layer-by-layer assembly technique. The resulting nanoporous structure is highly transparent and can be made both superhydrophobic and highly oleophobic after functionalization with a fluorocarbon molecule. We believe that the nanoporous textures form overhang structures on the coating surface, which induce the high oil-repellency of the coating even

though the intrinsic oil contact angle of the solid surface is less than 90°. Although transparent superhydrophobic coatings have been demonstrated using the layer-by-layer assembly technique previously, to the best of our knowledge, this is the first demonstration of fabricating transparent coatings that are both superhydrophobic and highly oleophobic.

6. We have used nanoparticle-polymer composites to demonstrate the anti-icing capability of superhydrophobic surfaces and report direct experimental evidence that such surfaces are able to prevent ice formation upon impact of supercooled water both in laboratory conditions and in natural environments. We find that the anti-icing capability of these composites depends not only on their superhydrophobicity but also on the size of the particles exposed on the surface. The critical particle sizes that determine the superhydrophobicity and the anti-icing property are in two different length scales. The effect of particle size on ice formation is explained by using a classical heterogeneous nucleation theory. This result implies that the anti-icing property of a surface is not directly correlated with the superhydrophobicity, and thus it is uncertain whether a superhydrophobic surface is anti-icing without detailed knowledge of the surface morphology. The result also opens up possibilities for rational design of anti-icing superhydrophobic surfaces by tuning surface textures in multiple length scales.
7. We have investigated interfacial slip on superhydrophobic surfaces and the resulting hydrodynamic drag reduction of laminar flows between two parallel plates through both numerical simulation and experimental approaches. It shows that slip length, a parameter commonly used to characterize the slippery nature of superhydrophobic surfaces, significantly decreases when the Reynolds number *Re* of laminar flows posed between

two superhydrophobic plates increases. When the resulting hydrodynamic drag reduction is described by the relative reduction R_f of a phenomenological friction factor, it is found that R_f has an empirical linear dependence on Re. Such a linear relationship may provide a convenient approach for calculating friction drag in hydrodynamic systems involving superhydrophobic surfaces.

APPENDIX

LAMINAR FLOW BETWEEN TWO INFINITE PARALLEL PLATES

Under an incompressible flow assumption for Newtonian fluids with constant ρ and μ, the typical *Navier-Stokes* equation is

$$\rho\left(\frac{\partial \vec{v}}{\partial t}+\vec{v}\cdot\nabla\vec{v}\right)=-\nabla p+\mu\nabla^2\vec{v}+\rho\vec{g}\ , \qquad \text{(A1)}$$

where ρ and μ are the density and viscosity of the liquid, respectively, and p is the pressure.

When a Newtonian fluid flows through two infinite parallel plates separated by a distance H, and the pressure drop is along x direction, Eqn.A1 may be expressed in the Cartesian coordinates (x, y, z) as

$$\rho\left(\frac{\partial v_x}{\partial t}+v_x\frac{\partial v_x}{\partial x}+v_y\frac{\partial v_x}{\partial y}+v_z\frac{\partial v_x}{\partial z}\right)=-\frac{\partial p}{\partial x}+\mu\left[\frac{\partial^2 v_x}{\partial x^2}+\frac{\partial^2 v_x}{\partial y^2}+\frac{\partial^2 v_x}{\partial z^2}\right]+\rho g_x\ . \quad \text{(A2)}$$

Because $v_x=v_x(y)$, p=p(x) and g_x=0, Eqn. A2 can be simplified to

$$0=-\frac{dp}{dx}+\mu\frac{d^2v_x}{dy^2}\ . \quad \text{(A3)}$$

It may be integrated to give

$$\frac{dv_x}{dy}=\frac{y}{\mu}\left(\frac{dp}{dx}\right)+C_1\ . \qquad \text{(A4)}$$

B.C. 1: at y=0, $\frac{dv_x}{dy} = \text{finite}$

Consequently C_1 must be zero. Therefore, the shear rate distribution is

$$\frac{dv_x}{dy} = \frac{y}{\mu}\left(\frac{dp}{dx}\right). \qquad \text{(A5)}$$

This first-order separable differential equation may be integrated to give

$$v_x = \frac{y^2}{2\mu}\left(\frac{dp}{dx}\right) + C_2 . \quad \text{(A6)}$$

In the case of no-slip boundary condition,

B.C. 2: at $y = \pm H/2, v_x$=0

From this, the C_2 is found to be $\left[\left(-\frac{dp}{dx}\right)_{no-slip}\frac{H^2}{8\mu}\right]$. Hence the velocity distribution is

$$v_x = \frac{1}{8\mu}\left(-\frac{dp}{dx}\right)_{no-slip}\left(H^2 - 4y^2\right). \quad \text{(A7)}$$

The average velocity U can be calculated from Eqn. A7

$$U = \frac{2\int_0^{H/2} v_x dy}{H} = \frac{H^2}{12\mu}\left(-\frac{dp}{dx}\right)_{no-slip}. \qquad \text{(A8)}$$

From Eqn. A 8,

$$\left(-\frac{dp}{dx}\right)_{no-slip} = \frac{12\mu U}{H^2} = \frac{6\mu^2\, Re}{\rho H^3}, \quad \text{(A9)}$$

where $Re = \frac{UD_h}{\nu}$ is the Reynolds number based on the hydraulic diameter (D_h is dependent on the cross sectional area, A, and the perimeter of the channel, P, by $D_h = 4A/P$. For the flow between the two infinite parallel plates, the channel height H is finite, while the channel width W is infinite. As a consequence, $D_h = 2(HW)/(H+W) \approx 2H$), average velocity U, and kinematic viscosity ($\nu = \mu/\rho$). The Darcy friction factor (f) for laminar flow can be calculated by Eqns A8 and A9:

$$f_{no-slip} = -2\left(\frac{dp}{dx}\right)_{no-slip}\frac{D_h}{\rho U} = \frac{96}{Re}, \qquad \text{(A10)}$$

However, when the interfacial slip occurs at the channel surface, the boundary conditions change to:

B.C. 2: $\quad$ at $y = H/2$, $v_x = -b\left(\frac{dv_x}{dy}\right)_{y=H/2}$ or $y = -H/2$, $v_x = b\left(\frac{dv_x}{dy}\right)_{y=H/2}$

where b is defined as slip length, and $\left(\frac{dv_x}{dy}\right)_{y=H/2} = -\left(\frac{dv_x}{dy}\right)_{y=-H/2} = \frac{H}{2\mu}\left(\frac{dp}{dx}\right)_{slip}$ calculated from Eqn A5.

From this new boundary condition, the C_2 in Eqn A6 can be found to be $\left[\frac{1}{2\mu}\left(-\frac{dp}{dx}\right)_{slip}\left(bH + \frac{H^2}{4}\right)\right]$. Hence the velocity distribution is

$$v_x = \frac{1}{8\mu}\left(-\frac{dp}{dx}\right)_{slip}\left(4bH + H^2 - 4y^2\right) \qquad \text{(A11)}$$

The average velocity U can be calculated from Eqn. A11

$$U = \frac{2\int_0^{H/2} v_x dy}{H} = \frac{H^2}{12\mu}\left(1+\frac{6b}{H}\right)\left(-\frac{dp}{dx}\right)_{slip} \quad . \quad \text{(A12)}$$

From Eqn A12,

$$\left(-\frac{dp}{dx}\right)_{slip} = \frac{12\mu U}{H^2\left(1+\frac{6b}{H}\right)} = \frac{6\mu^2 Re}{\rho H^3\left(1+\frac{6b}{H}\right)} . \qquad \text{(A13)}$$

The Darcy friction factor can be calculated by Eqn A13

$$f_{slip} = -2\left(\frac{dp}{dx}\right)_{slip}\frac{D_h}{\rho U} = \frac{96}{Re}\left(\frac{1}{1+\frac{6b}{H}}\right). \qquad \text{(A14)}$$

BIBLIOGRAPHY

1. R. Blossey, Self-cleaning surfaces- virtual realities. *Nature Mater.* **2003**, 2, 301-306.

2. L. Feng, S. Li, Y. Li, H. Li, L. Zhang, J. Zhai, Y. Song, B. Liu, L. Jiang, and D. Zhu, Super-hydrophobic surfaces: From natural to artificial. *Adv. Mater.* **2002**, 14, 1857-1860.

3. R. Furstner, W. Barthlott, C. Neinhuis and P. Walzel, Wetting and Self-cleaning Properties of Artificial Superhydrophobic surfaces. *Langmuir* **2005**, 21, 956-961.

4. X. F. Gao, and L. Jiang, Water-repellent legs of water striders. *Nature* **2004**, 432, 36-36.

5. W. Lee, M.K. Jin, W.C. Yoo, and J. K. Lee, Nanostructuring of a polymeric substrate with well-defined nanometer-scale topography and tailored surface wettability. *Langmuir* **2004**, 20, 7665-7669.

6. J. N. Israelachvili, Intermolecular and Surface Forces, 2nd ed.; Academic Press: New York, 1991; pp 144-145.

7. S. Shibuichi, T. Yamamoto, T. Onda, and K. Tsujii, Super water- and oil-repellent surfaces resulting from fractal structure. *J. Colloid Interface Sci.***1998**, 208, 287-294.

8. R.N. Wenzel, Resistance of solid surfaces to wetting by water. *Ind. Eng. Chem.* **1936**, 28, 988-994.

9. A.B.D. Cassie, and S. Baxter, Wettability of porous surfaces. *Trans. Faraday Soc.* **1944**, 40, 546-551.

10. D. Quéré, Non-sticking drops. *Rep. Prog. Phys.* **2005**, 68, 2495-2532.

11. J. Bico, U. Thiele, and D. Quéré, Wetting of textured surfaces. *Colloids Surf. A* **2002**, 206, 41-46.

12. C.G.L. Furmidge, Studies at phase interfaces. I. The sliding of liquid drops on solid surfaces and a theory for spray retention. *J. Colloid Sci.* 1962, 17, 309-324.

13. T. Onda, S. Shibuichi, N. Satoh, and K. Tsujii, Super-Water-Repellent Fractal Surfaces. *Langmuir* 1996, 12, 2125-2127.

14. M. Jin, X. Feng, J. Xin, J. Zhai, K. Cho, L. Feng, and L. Jiang, Super-hydrophobic PDMS surface with ultra-low adhesive force. *Macromol. Rapid Commun.* 2005, 26, 1805-1809.

15. M. Ma, R. M. Hill, J. L. Lowery, S. V. Fridrikh, and G. C. Rutledge, Electrospun poly(styrene-block-dimethylsiloxane) block copolymer fibers exhibiting superhydrophobicity. *Langmuir* 2005, 21, 5549-5554.

16. H. Y. Erbil, A. L. Demirel, Y. Avci, and O. Mert, Transformation of a simple plastic into a superhydrophobic surface. *Science* 2003, 299, 1377-1380.

17. L. Zhang, Z. Zhou, B. Cheng, J. M. DeSimone, and E. T. Samulski, Superhydrophobic behavior of a perfluoropolyether lotus-leaf-like topography. *Langmuir* 2006, 22, 8576-8580.

18. H. Yan, K. Kurogi, H. Mayama, and K. Tsujii, Environmentally stable super water-repellent poly(alkylpyrrole) films. *Angew. Chem. Int. Ed.* 2005, 44,3453-3456.

19. X. Feng, L. Feng, M. Jin, J. Zhai, L. Jiang, and D. Zhu, Reversible superhydrophobicity to superhydrophilicity transition of aligned ZnO nanorod films. *J. Am. Chem. Soc.* 2004, 126, 62-63.

20. X. Feng, J. Zhai, and L. Jiang, The fabrication and switchable superhydrophobicity of TiO_2 nanorod films. *Angew. Chem. Int. Ed.* 2005, 44, 5115-5118.

21. D. Oner, and T. J. McCarthy, Ultrahydrophobic surfaces. Effects of topography length scales on wettability. *Langmuir* 2000, 16, 7777-7782.

22. T. Baldacchini, J. E. Carey, M. Zhou, and E. Mazur, Superhydrophobic surfaces prepared by microstructuring of silicon using a femtosecond laser. *Langmuir* 2006, 22, 4917-4919.

23. N. Verplanck, E. Galopin, J. Camart, and V. Thomy, Reversible electrowetting on superhydrophobic silicon nanowires. *Nano lett.* 2007, 7, 813-817.

24. B. Qian, and Z. Shen, Fabrication of superhydrophobic surfaces by dislocation-selective chemical etching on aluminum, copper, and zinc substrates. *Langmuir* 2005, 21, 9007-9009.

25. X. Zhang, F. Shi, X. Yu, H. Liu, Y. Fu, Z. Wang, L. Jiang, and X. Li, Polyelectrolyte multilayer as matrix for electrochemical deposition of gold clusters: toward superhydrophobic surface. *J. Am. Chem. Soc.* 2004, 126, 3064-3065.

26. N. Zhao, F. Shi, Z. Wang, and X. Zhang, Combining layer-by-layer assembly with electrodeposition of silver aggregates for fabricating superhydrophobic surfaces. *Langmuir* 2005, 21, 4713-4716.

27. K. Tsujii, T. Yamamoto, T. Onda, and S. Shibuichi, Super oil-repellent surfaces. *Angew. Chem., Int. Ed. Engl.* 1997, 36, 1011-1012.

28. S. Shibuichi, T. Yamamoto, T. Onda, and K. Tsujii, Super water- and oil-repellent surfaces resulting from fractal structure. *J. Colloid Interface Sci.* 1998, 208, 287-294.

29. C. Neinhuis, and W. Barthlott, Characterization and distribution of water-repellent, self-cleaning plant surfaces. *Ann. Bot.* 1997, 79, 667-667.

30. Y. T. Cheng, and D. E. Rodak, Is the lotus leaf superhydrophobic? *Appl. Phys. Lett.* 2005, 86, 144101.

31. http://www.surface-tension.de/

32. A. Lafuma, and D. Quéré, Superhydrophobic states. *Nature Mater.* 2003, 2, 457-460.

33. A. Marmur, The lotus effect:superhydrophobicity and metastability. *Langmuir* 2004, 20, 3517-3519.

34. B. He, N. A. Patankar, and J. Lee, Multiple equilibrium droplet shapes and design criterion for rough hydrophobic surfaces. *Langmuir* 2003, 19, 4999-5003.

35. C. Ishino, K. Okumura, and D. Quéré, Wetting transitions on rough surfaces. *Europhys Lett.* 2004, 68, 419-425.

36. S. Herminghaus, Roughness-induced non-wetting. *Europhys. Lett.* 2000, 52, 165-170.

37. J. Westwater, D. P. Gosain, S. Tomiya, S. Usui, and H. Ruda, Growth silicon nanowires via gold/silane vapor-liquid-solid reaction. *J. Vac. Sci. Technol. B* 1997, 15, 554.

38. D. Gao, R. He, C. Carraro, R. T. howe, P. Yang, and R. Maboudian, Selective growth of Si nanowire arrays via galvanic displacement processes in water-in-oil microemulsions. *J. Am. Chem. Soc.* 2005, 127, 4574-4575.

39. M. R. Houston, and R. Maboudian, Stability of ammonium fluoride-treated Si (100). *J. Appl. Phys.* 1995, 78, 3801-3808.

40. A. Tuteja, W. Choi, M. Ma, J. M. Mabry, S. A. Mazzella, G. C. Rutledge, G. H. McKinley, and R. E. Cohen, Designing superoleophobic surfaces. *Science* 2007, 318, 1618-1622.

41. L. Zhong, J. Hu, H. Liang, A. Cao, W. Song, and L. Wan, Self-assembled 3D flowerlike iron oxide nanostructures and their application in water treatment. *Adv. Mat.* 2006, 18, 2426-2431.

42. S. M. Iveson, S. Holt, and S. Biggs, Advancing contact angle of iron ores as a function of their hematite and goethite content: implications for pelletising and sintering. *Int. J. Miner. Process.* 2004, 74, 281-287.

43. Y. Li, Y. Bando, and D. Golberg, MoS_2 nanoflowers and their field-emission properties. *Appl. Phys. Lett.* 2003, 82, 1962-1964.

44. Y. Zhao, D. Ye, G. Wang, and T. Lu, Novel nano-column and nano-flower arrays by glancing angle deposition. *Nano. Lett.* 2002, 2, 351-354.

45. Z. Wang, X. F. Qian, J. Yin, and Z. Zhu, Large-scale fabrication of tower-like, flower-like, and tube-like ZnO arrays by a simple chemical solution route. *Langmuir* 2004, 20, 3441-3448.

46. K. Peng, J. Hu, Y. Yan, Y. Wu, H. Fang, Y. Xu, S. Lee, and J. Zhu, Fabrication of single-crystalline silicon nanowires by scratching a silicon surface with catalytic metal particles. *Adv. Funct. Mater.* 2006, 16, 387-394.

47. J. Bravo, L. Zhai, Z. Wu, R. E. Cohen, and M. F. Rubner, Transparent superhydrophobic films based on silica nanoparticles, *Langmuir* 2007, 23, 7293-7298.

48. Y. Li, F. Liu, and J. Sun, A facile layer-by-layer deposition process for the fabrication of highly transparent superhydrophobic coatings. *Chem. Commun.* 2009, 23, 2730-2732.

49. Y. H. Xiu, F. Xiao, D. W. Hess, and C. P. Wong, Superhydrophobic optically transparent silica films formed with a eutectic liquid. *Thin Solid Films* 2009, 517, 1610-1615.

50. G. R. J. Artus, S. Jung, J. Zimmermann, H. –P. Gautschi, K. Marquardt, and S. Seeger, Silicone nanofilaments and their application as superhydrophobic coatings. *Adv. Mater.* 2006, 18, 2758-2762.

51. L. Cao, T. P. Price, M. Weiss, and D. Gao, Super water- and oil-repellent surfaces on intrinsically hydrophilic and oleophilic porous silicon films. *Langmuir* 2008, 24, 1640-1643.

52. L. Cao, H. Hu, and D. Gao, Design and fabrication of micro-textures for inducing a superhydrophobic behavior on hydrophilic materials. *Langmuir* 2007, 23, 4310-4314.

53. A. Cao, L. Cao, and D. Gao, Fabrication of nonaging superhydrophobic surfaces by packing flowerlike hematite particles. *Appl. Phys. Lett.* 2007, 91, 034102.

54. H. Saito, K. Takai, and G. Yamauchi, Water- and ice-repellent coatings. *Surf. Coat. Int.* 1997, 80, 168-171.

55. A. Nakajima, K. Hashimoto, and T. Watanabe, Recent studies on super-hydrophobic films. *Monatsh. Chem.* 2001, 132, 31-41.

56. S.A. Kulinich, and M. Farzaneh, Ice adhesion on super-hydrophobic surfaces. *Appl. Surf. Sci.* 2009, 255, 8153-6157.

57. S. G. Cober, G. A. Isaac, and J. W. Strapp, Characterizations of aircraft icing environments that include supercooled large drops. *J. Appl. Meteorol.* 2001, 40, 1984-2002.

58. S. Lasher-Trapp, S. Anderson-Bereznicki, A. Shackelford, C. H. Twohy, and J. G. Hudson, An investigation of the influence of droplet number concentration and giant aerosol particles upon supercooled large drop formation in wintertime stratiform clouds. *J. Clim. Appl. Meteorol.* 2008, 47, 2659-2678.

59. X. Liu, A new kinetic model for three-dimensional heterogeneous nucleation. *J. Chem. Phys.* 1999,111, 1628-1635.

60. W. M. Ketcham, and P. V. Hobbs, An experimental determination of surface energies of ice. *Philos. Mag.* 1969, 19, 1161-1173.

61. C. Neto, D. R. Evans, E. Bonaccurso, H. J. Butt, and V. S. J. Craig, Boundary slip in Newtonian liquids: a review of experimental studies. *Rep. Prog. Phys.* 2005, 68, 2859-2897.

62. O. I. Vinogradova, Drainage of a thin liquid-film confined between hydrophobic surfaces. *Langmuir* 1995, 11, 2213-2220.

63. O. I. Vinogradova, Slippage of water over hydrophobic surfaces. *Int. J. Miner. Process* 1999, 56, 31-60.

64. P. G. de Gennes, On fluid/wall slippage. *Langmuir* 2002, 18, 3413-3414.

65. Y. Zhu, and S. Granick, Rate-dependent slip of Newtonian liquid at smooth surfaces. *Phys. Rev. Lett.* 2001, 87, 096105.

66. S. Granick, Y. Zhu, and H. Lee, Slippery questions about complex fluids flowing past solids. *Nat. Mater.* 2003, 2, 221-227.

67. D. C. Tretheway, and C. D. Meinhart, A generating mechanism for apparent fluid slip in hydrophobic microchannels. *Phys. Fluids* 2004, 16, 1509-1515.

68. K. Watanabe, Y. Udagawa, and H. Udagawa, Drag reduction of Newtonian fluid in a circular pipe with a highly water-repellent wall. *J. Fluid Mech.* 1999, 381, 225-238.

69. K. Watanabe, T. Takayama, S. Ogata, and S. Isozaki, Flow between two coaxial rotating cylinders with a highly water-repellent wall. *AIChE J.* 2003, 49, 1956-1963.

70. J. Ou, J. B. Petrot, and J. P. Rothstein, Laminar drag reduction in microchannels using ultrahydrophobic surfaces. *Phys. Fluids* 2004, 16, 4635-4643.

71. N. J. Shirtcliffe, G. McHale, M. I. Newton, and Y. Zhang, Superhydrophobic copper tubes with possible flow enhancement and drag reduction. *ACS Appl. Mater. Interface* 2009, 1, 1316-1323.

72. S. Gogte, P. Vorobieff, R. Truesdell, A. Mammoli, F. van Swol, P. Shah, and C. J. Brinker, Effective slip on textured superhydrophobic surfaces. *Phys. Fluids* 2005, 17, 051701.

73. R. Truesdell, A. Mammoli, P. Vorobieff, F. van Swol, and C. J. Brinker, Drag reduction on a patterned superhydrophobic surface. *Phys. Rev. Lett.* 2006, 97, 044504.

74. C. H. Choi, and C. J. Kim, Large slip of aqueous liquid flow over a nanoengineered superhydrophobic surface. *Phys. Rev. Lett.* 2006, 96, 066001.

75. C. H. Choi, U. Ulmanella, J. Kim, C. M. Ho, and C. J. Kim, Effective slip and friction reduction in nanograted superhydrophobic microchannels. *Phys. Fluids* 2006, 18, 087105.

76. C. Navier, Memoire sur les lois du movement des fluids. *Memoires de l' Academie Royale des Sciences de l'Institut de France* 1823, 6, 389-416.

77. P. Joseph, C. Cottin-Bizonne, J. M. Benoit, C. Ybert, C. Journet, P. Tabeling, and L. Bocquet, Slippage of water past superhydrophobic carbon nanotube forests in microchannels. *Phys. Rev. Lett.* 2006, 97, 156104.

78. C. Lee, C. H. Choi, and C. J. Kim, Structured surfaces for a giant liquid slip. *Phys. Rev. Lett.* 2008, 101, 064501.

79. R. D. Blevins, Applied Fluid Dynamics Handbook (Van Nostrand Reinhold, New York, 1984).

80. L. Cao, A. K. Jones, V. K. Sikka, J. Wu, and D. Gao, Anti-icing superhydrophobic coatings, *Langmuir* 2009, 25, 12444-12448.

81. S. S. Sadhal, P. S. Ayyaswamy, and J. N. Chung, Transport phenomena with drops and bubbles (Springer Verlag, 1997)